LARGE-EDDY SIMULATION OF TURBULENT WALL-PRESSURE FLUCTUATIONS USING THE FINITE ELEMENT METHOD

By

Jhiin Joo

Kidambi Sreenivas
Associate Professor of Mechanical Engineering
(Chair)

James C. Newman III
Professor and Department Head of Mechanical Engineering
(Committee Member)

Timothy W. Swafford
Professor Emeritus of Computational Science
(Committee Member)

John V. Matthews III
Professor of Mathematics
(Committee Member)

LARGE-EDDY SIMULATION OF TURBULENT WALL-PRESSURE FLUCTUATIONS USING THE FINITE ELEMENT METHOD

By

Jhiin Joo

A Dissertation Submitted to the Faculty of the University of Tennessee at Chattanooga in Partial Fulfillment of the Requirements of the Degree of Doctor of Philosophy in Computational Engineering

The University of Tennessee at Chattanooga
Chattanooga, Tennessee

August 2019

ABSTRACT

In the present dissertation, turbulent wall-pressure fluctuations are characterized. To capture the turbulent characteristics of the flow, large-eddy simulation is used to resolve the large scale motions of the flow directly. A wall-adapting local eddy-viscosity model is selected to account for the effect of small scale motions. The streamwise/upwind Petrov-Galerkin method is chosen to discretize the computational domain and a second-order backward difference formula is applied for the time integration. Maintaining turbulent flow throughout the simulation domain to properly characterize turbulence is critical in investigating wall-pressure fluctuations. In order to reduce the size of the simulation domain an inflow generation method, a variant of the recycling and rescaling method, is used. In this method, the turbulent velocity profile from a specific plane within the computational domain is recycled and rescaled appropriately, and re-introduced at the inlet of the domain at every time step iteration. In the proposed method, the mean velocity profile is fixed at the inlet while the velocity fluctuations are recycled and rescaled to obtain the desired turbulent characteristics. This method is simple and effective and maintains the turbulent flow throughout the simulation domain. The non-reflecting boundary conditions with a sponge layer are applied at the top and exit of the computational domain to remove unwanted reflections from the boundary. In order to examine the present inflow generation method and the ability to capture the wall-pressure fluctuations, numerical results are verified on a flat plate with a zero pressure gradient. The mean velocity profile, the RMS velocity fluctuations, and the friction velocity over time

are investigated to show the effectiveness of the present inflow turbulent generation method. Computed wall-pressure fluctuations are evaluated using the time-averaged statistics and the spectra, to show that they are characterized well using the present method.

DEDICATION

This work is dedicated to my fiancé, whom I love so much from the bottom of my heart, my family: my mother, who loves me and always prays for me, my precious sister and brother, for their love and support, and my father, who is in heaven now and to the Wong family.

ACKNOWLEDGEMENTS

I would like to first acknowledge my advisor, Dr. Kidambi Sreenivas, for his wonderful guidance, patience, and encouragement along the way. Without his presence and help, I would not have been able to complete this journey. I would also like to express my sincere appreciation to Dr. Timothy W. Swafford, for giving me this valuable opportunity to study at the SimCenter and for his continuous support and encouragement. I would like to thank Dr. James C. Newman III for his outstanding teaching and his care for students. I would also like to express my appreciation to Dr. John V. Matthews III for willingly serving as my committee member. Last but not least, I am very thankful for Kim who has always been there as my mom at the SimCenter, and Ethan for his support and help.

TABLE OF CONTENTS

LIST OF TABLES

LIST OF FIGURES

CHAPTER 1

INTRODUCTION

The airplane has become one of the most important means of transportation in this generation mainly due to its ability to travel long distances in short transport times. However, it has a lot of problems including aircraft noise. Aircraft interior cabin noise has become a serious aircraft noise problem as it directly affects passenger comfort and health. Numerous experimental and numerical approaches have been utilized by researchers to find the main cause of this problem. Alaoui [1] notes that a turbulent boundary layer that is generated on the fuselage as the aircraft moves through the air is one of the main sources of aircraft interior noise. Blake [2] mentions in his book that the pressure fluctuations caused by a turbulent boundary layer are responsible for structural vibrations that are transmitted through the structure. These are well demonstrated in Figure 1.1. In fact, the noise generated by airflow over the aircraft surfaces is important for all scales - from small to the large ones [3]. Kraichnan [4] also mentioned that the pressure fluctuations within a turbulent boundary layer exert a force on the surface which results in the transmission of noise. He pointed out the importance of investigating the structure of this driving force distribution.

As air with nonzero viscosity passes the fixed surface, a thin region near the wall (solid surface) is formed where the velocity varies from zero at the wall to the freestream velocity away from the wall. This region is called the boundary layer. Boundary layers can be laminar or turbulent depending on the Reynolds number. For practical problems, flows with higher Reynolds numbers

will usually result in turbulent boundary layers. They are characterized by unsteady motion of the flow within the boundary layer. This is illustrated in Figure 1.2.

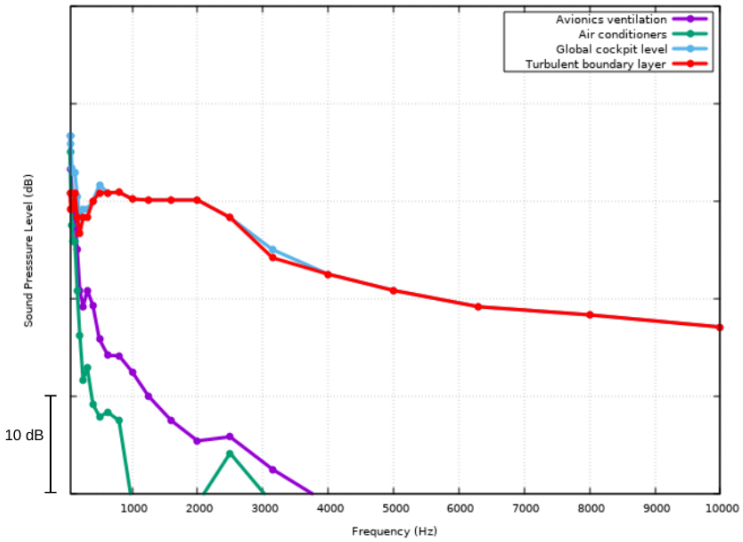

(a) Noise sources in an A380 cockpit - Airbus document [1]

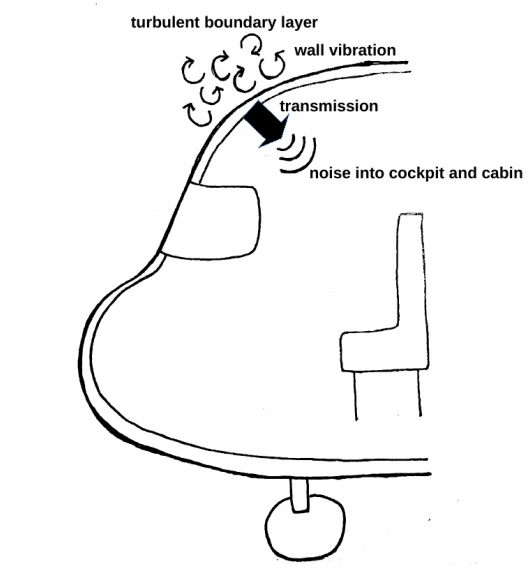

(b) Noise generated by flow

Figure 1.1 Noise sources in an A380 cockpit - Airbus document [1] and the illustration of noise caused by flow

As can be seen from Figure 1.2, a turbulent boundary layer consists of an inner and an outer layer with an intermediate overlap region between the two [5]. In the inner layer, viscous effects are dominant and the velocity profile has a linear variation. The turbulent eddy shear dominates in the outer layer and the velocity profile has a logarithmic variation as shown in Figure 1.3.

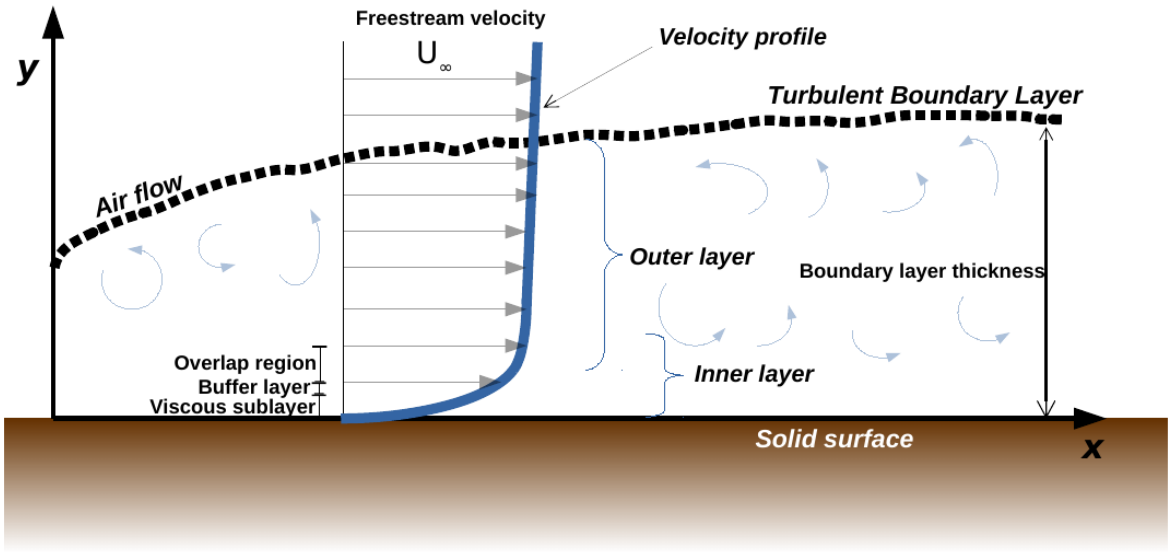

Figure 1.2 Illustration of turbulent boundary layer

In order to reduce the undesired aerodynamic noise and structural vibration caused by a turbulent boundary layer on the aircraft, accurate and detailed information concerning the behavior of wall-pressure fluctuations in the external turbulent boundary layer is necessary. Considerable amount of experiments and theoretical approaches have been developed by researchers to gain more insight into the surface-pressure fluctuations. More recently, an increase in computational power has led to improved accuracy and better resolution of the flow field which can be achieved

using appropriate numerical methods to solve the specific governing equations in less time than ever before.

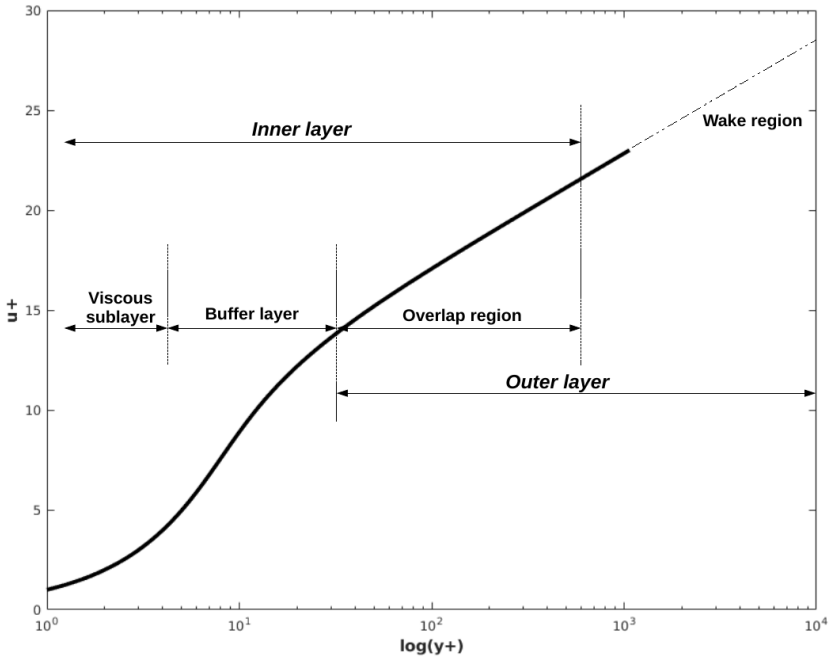

Figure 1.3 The universal law of the wall by Spalding [5] with different regions of turbulent boundary layer

Accurately capturing the behavior of turbulent flow using numerical methods can help reduce the resources needed to perform experiments, thereby saving time and money. In this thesis, a finite element formulation, applied to a large-eddy simulation, is utilized to capture the behavior of wall-pressure fluctuations. This information can then be passed on to the next level toward the ultimate goal, which is to reduce the noise and vibration of the aircraft caused by the turbulent boundary layer.

1.1 Literature Review

The study of the behavior of wall-pressure fluctuations has been investigated for more than fifty years. Most of the studies are performed based on experimental measurements using an array of pinhole microphones in a wind-tunnel. The previous works in this subject in the literature are shown in this section.

Back in 1950s, when less was known about the characteristics of the turbulent boundary layer, Kraichnan [4] analyzed qualitatively the pressure fluctuation structure due to turbulent boundary layer over a smooth surface. In his work, he used the similarity arguments to estimate the approximate dependence of the mean-square intensity, spatial scale, and frequency scale on Mach number and distance from where the boundary layer transitions from laminar to turbulent flow. He also constructed an idealized model of turbulent boundary layer flow and used it to relate the spectrum and correlation function of the surface pressure distribution to the corresponding functions of a homogeneous turbulent flow.

Phillips [6] investigated the properties of the sound generated by the turbulent pressure fluctuations on a rigid surface from a turbulent boundary layer. He assumed that the fluid is incompressible, and that the turbulence was homogeneous in planes parallel to an infinite plane boundary. He suggested that in that case the sound radiation vanishes with increasing distance down the plate.

Willmarth and Wooldridge [7] performed an experimental study to measure the turbulent pressure field at the wall beneath a thick turbulent boundary layer. They noticed that the previous investigations of the wall-pressure fluctuations were limited due to the relatively large size of pressure transducers. They attempted to increase the accuracy of the experimental information

by devising experiments beneath a thick turbulent boundary layer. Their results showed that the low-frequency pressure fluctuations have the highest convection speed in a fully turbulent flow. They also showed that the transverse and longitudinal scales of both the large and small pressure-producing eddies are of the same order of magnitude.

Corcos, in [8] and [9], used the measurements of Willmarth and Wooldridge [7] to develop a correction to account for the attenuation of the frequency-spectral density of the boundary layer due to the poor transducer resolution and suggested the appropriate scale factor of the pressure field. He also claimed that the source terms are an important part of the pressure of a turbulent boundary layer at the wall by analyzing the data of Willmarth and Wooldridge [7].

In 1970, Blake [10] used microphones three times smaller than the ones used in earlier works in a low-noise wind tunnel facility to make accurate turbulent boundary layer wall-pressure measurements. He compared the measurements of the pressure fluctuations for smooth and rough wall boundary layers. He mentioned that the wall-pressure source location is determined as the position in the boundary layer for which the convection velocity is identical to the mean velocity. Additionally, he concluded that the high-frequency pressure levels are determined by length and velocity scales characteristic of the region where pressure sources for these levels are located. His smooth-wall data agreed well with the measurements of Willmarth and Wooldridge [7] and Corcos [8, 9]. He also mentioned that the roughness separation affected the very large-scale structure, whereas the roughness height influenced the medium and very small-scale turbulence.

The measurements of pressure fluctuations within the boundary layer had unavoidable measurement error until the early 1970s due to the relatively large size of transducers. This is pointed

out in [11] as Willmarth gave a comprehensive review of knowledge about pressure fluctuations beneath turbulent boundary layers in 1975.

Increases in computational power has allowed for direct numerical simulation techniques to be applied to the study of wall-pressure fluctuations. Kim [12] calculated the pressure fluctuations by analyzing a database obtained using direct numerical simulation in a turbulent channel flow. He decomposed the pressure into rapid and slow parts corresponding to the linear and nonlinear source terms, respectively, in the Poisson equation. It was believed before Corcos [9] that the contribution of the slow pressure term to the Poisson equation is negligible. However, Kim [12] confirmed that the slow pressure term could not be neglected near the wall and in fact, was larger away from the wall. He also found that the major contribution to the mean-square wall-pressure fluctuations came from the region where the mean-square of the nonlinear source terms peak. He calculated and discussed the probability density distribution, the power spectra and two-point correlations of the pressure fluctuations in a turbulent channel flow.

Choi and Moin [13] computed the three-dimensional frequency/wavenumber spectrum of wall-pressure fluctuations using a database obtained by direct numerical simulation of turbulent channel flow. It was shown that the outer variables were the appropriate scaling for the spectra at low frequency, and the inner variables for the high-frequency range pressure fluctuations. They also calculated the convection velocities of pressure fluctuations as a function of frequency, wavenumber, and spatial and temporal separations.

Farabee and Casarella [14] performed experimental measurements of the frequency spectra and frequency cross-spectra of the wall pressure fluctuations beneath a fully developed turbulent boundary layer. They identified through their measurements of the turbulent source regions within

the boundary layer that contribute to the low, mid, and high frequency ranges of the wall pressure field. They also identified the characteristic features of the data in the low-frequency range for which data were lacking. Their convection velocity data showed that the major turbulent contributions to the low and high wavenumber groups came from the outer and inner layers, respectively. Their results also indicated the sensitivity of the wall pressure field to enriched organized structures in the outer flow.

Singer [15] made an effort to understand the behavior of wall-pressure fluctuations in the external turbulent boundary layer, which produces unwanted vibration and noise in the interior cabin of the aircraft numerically in 1996. He performed calculations for an incompressible flat-plate turbulent boundary layer using large-eddy simulations with a zero pressure gradient to investigate the structure of wall-pressure fluctuations of an aircraft fuselage. He presented the results on the statistical properties of the wall-pressure fluctuations such as the distribution of wall-pressure, coherence of the time-averaged two-point correlations, frequency spectra, and the coherence of the cross-spectral density functions that matched well with those of previous experiments and calculations.

Chang et al. [16] investigated the velocity-field and pressure databases obtained from a direct numerical simulation of incompressible, fully developed, turbulent channel flow. They found that the buffer region of the boundary layer dominates most of the wavenumber range. They noted that the viscous shear layer is significant at high wavenumbers, whereas the buffer and logarithmic regions are important at the low wavenumber. They further investigated the rapid and slow parts mentioned in the work of Kim [12], which indicate the linear and nonlinear terms of the source

terms in a Poisson's equations, respectively, and found that these two partial pressures are the same order of magnitude, having the same shape as the total pressure.

In an effort to reduce computational costs, Wang [17] developed a cost-effective hybrid large-eddy simulation and wall-modeling approach for surface pressure fluctuations. His method predicted low-order velocity statistics in very good agreement with large-eddy simulation results. Goody [18] proposed an empirical model with a simple function of the ratio of the timescales of the outer to inner boundary layer. He presented the surface pressure spectra beneath a two-dimensional, zero-pressure gradient boundary layer that agreed well with experimental data.

Lee et al. [19] obtained turbulent flow fields from solving the Reynolds Averaged Navier-Stokes equations, for flows over a backward-facing step. Their results agreed well with measurements in the redeveloped boundary layer region downstream of the reattachment zone.

More recently, Mahmoudnejad et al. [20] estimated wall pressure fluctuations using detached eddy simulation based on the Spalart-Allmaras turbulence model (DES-SA) and observed that the general trend in mid and high frequency regions is similar to Goody's model, whereas their results in the low frequency region are higher than the model's prediction.

The finite element method is one of several numerical methods that can be used to solve the governing equations and it can be applied to numerous engineering problems. It has a rigorous mathematical and physical foundation that is provable to be convergent and applicable to realistic real world problems. Moreover, introducing higher-order accurate methods is very straightforward in the finite element method formulation. The higher-order finite element method has gained the attention in the past few decades especially for problems requiring high accuracy.

Although the accuracy is critical in analyzing the wall-pressure fluctuations on the solid surface and computational power has been increasing, to the best of the author's knowledge, there has not been a simple method published for investigating the wall-pressure fluctuations using large-eddy simulations and the finite element method formulation. Furthermore, to date, large-eddy simulations using a wall-adapting local eddy viscosity model as a subgrid scale model has not been applied to this problem. In this thesis, the behavior of turbulent wall-pressure fluctuations using the finite element method formulation and large-eddy simulation is presented.

1.2 Outline

In the following chapters, the numerical methods to solve the governing equations are described, along with the results. Chapter 2 presents large-eddy simulations as the filtered compressible Navier-Stokes equations and a wall-adapting local eddy-viscosity model. Chapter 3 depicts in detail the Streamwise/Upwind Petrov-Galerkin discretization and the temporal discretization used in this thesis. Chapter 4 introduces the inflow turbulence generation method, including the literature reviews on this subject and the actual method used in this work. The statistical quantities are presented and explained in Chapter 5 and the numerical results of the inflow turbulent generation method and statistics are presented and discussed in Chapter 6. Chapter 7 concludes this thesis and presents suggestions for the future work.

CHAPTER 2

GOVERNING EQUATIONS AND SUBGRID SCALE MODELING

Most of the real fluid flows in engineering applications are turbulent. However, a precise characterization of turbulence can probably never be achieved, due to its complexity.

When Werner Heisenberg, a German theoretical physicist, was asked what he would ask God, he said: "*When I meet God, I am going to ask him two questions: Why relativity? And why turbulence? I really believe he will have an answer for the first.*" [21] Similarly, Horace Lamb, an English applied mathematician and fluid dynamicist, was quoted: "*I am an old man now, and when I die and go to heaven there are two matters on which I hope for enlightenment. One is quantum electrodynamics, and the other is the turbulent motion of fluids. And about the former I am rather optimistic.*" [22]

Turbulence can only be defined by its physical features or characteristics such as: a high Reynolds number flow phenomenon involving interactions between the nonlinear inertial terms and viscous terms, an irregular or random flow pattern, its inherently diffusive nature, both rotational and three dimensional, and dissipative nature, etc. [23]. One visualization of turbulent flow over a flat plate is taken from [24] and is shown in Figure 2.1 where the complexity of the flow is evident.

Furthermore, turbulence has a wide range of time and length scales. They can be represented by frequencies and wavelengths by a Fourier analysis of a turbulent-flow time history [24]. The illustration of energy spectrum in turbulent flow is shown in Figure 2.2.

The larger-scale turbulent motion with low wavenumbers carries most of the turbulent kinetic energy. These larger eddies cascade the kinetic energy contained in the energy production region to the smaller ones in the inertial range. Small eddies dissipate the energy they receive from larger eddies in the spectrum.

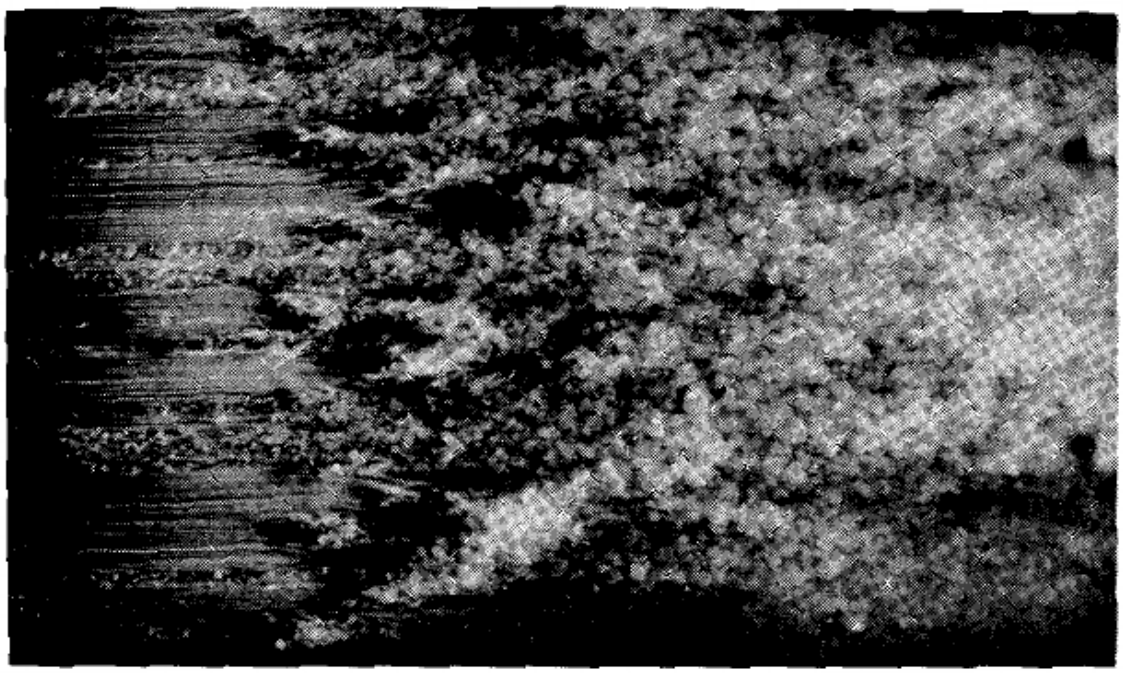

(a)

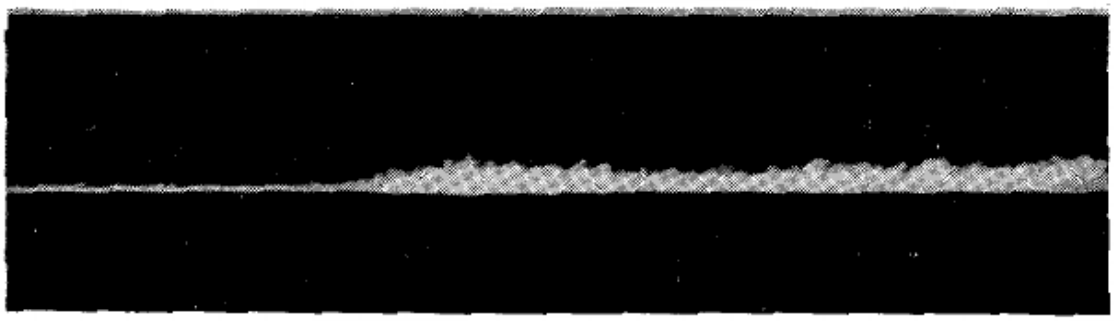

(b)

Figure 2.1 Smoke visualization of air flow past a flat plate: (a) top view and (b) side view [24]

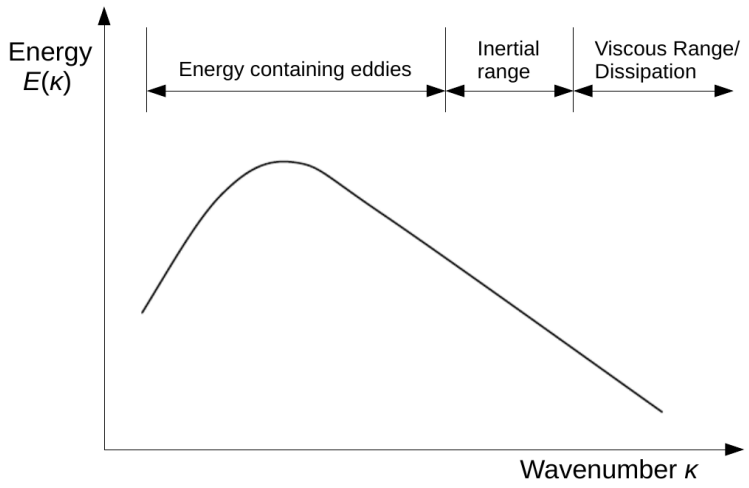

Figure 2.2 Turbulent energy spectrum: log-log scale

The difficulty in turbulence modeling arises from the requirement that contributions from all scales in the spectrum be represented accurately. The main approaches for computing turbulent flow include Direct Numerical Simulation (DNS), Large-eddy Simulation (LES), and Reynolds-averaged Navier-Stokes (RANS). DNS solves the Navier-Stokes equations directly to capture all physically important scales from the largest to the smallest ones. Even though this approach is the most representative of Mother Nature (i.e., no modeling is used), it requires a very fine mesh and is computationally very expensive. This makes DNS impractical for even fairly simple cases. In the RANS approach, only the time-averaged mean-flow variables are computationally resolved and the fluctuating quantities in Reynolds stress terms are modeled by semi-empirical approximations; for examples one-equation (Spalart-Allmaras), or two-equation (k-ϵ, k-ω, SST, etc.) models. As the variables are averaged in time, RANS is not capable of resolving the unsteady flow structure of turbulence. LES solves only the large scale motions, and the small scale motions are modeled using

an appropriate subgrid scale model. Therefore, one can imply that LES sits between RANS and DNS, relative to the accuracy of their representation of the physics and the computational costs.

LES is used in this work, because it is more representatives of the physics in resolving turbulent behavior than the RANS approach and is still notably cheaper computationally than DNS. As mentioned above, in LES, the large eddies are directly resolved, and the small eddies are modeled using a subgrid scale model. Different models have been developed to deal with the subgrid-scale motion, and the WALE model [25] is investigated in this work. WALE is discussed in Section 2.2.

Wang et al. [26] have investigated multiscale LES using a high-order discontinuous Galerkin finite element method using the WALE model. The LES algorithm and WALE model explained in this chapter is based on their work.

2.1 Governing Equations

As mentioned above, the large-scale and small-scale motion are treated differently in LES. The large scales are resolved directly, whereas the small scales are modeled by the appropriate subgrid-scale turbulence model. Therefore, a filtering operation is first required for the LES method, so that it can divide the turbulent spectrum into the large-scale resolved motion and smaller-scale unresolved motion. The filtering operation decomposes the flow variable into resolved (filtered) and unresolved components. The Favre filtering operation [27] is used for filtering in this work. For a function f, the Favre-filtered form is defined to be $\tilde{f} = \overline{\rho f}/\overline{\rho}$ where the overbar represents a time averaged quantity. The Favre filtering operation can be thought of as a density weighted filter in space. It is worth noting that, in general, the Favre filter does not commute with the temporal differential operator ∂_t and the spatial differential operator ∂_j.

Applying this filtering operation to the non-dimensional form of the three-dimensional compressible Navier-Stokes equations, the filtered three-dimensional compressible Navier-Stokes equations are:

$$\frac{\partial \overline{\rho}}{\partial t} + \frac{\partial}{\partial x_j}\left(\overline{\rho}\tilde{u}_j\right) = 0 \tag{2.1}$$

$$\frac{\partial}{\partial t}\left(\overline{\rho}\tilde{u}_i\right) + \frac{\partial}{\partial x_j}\left(\overline{\rho}\tilde{u}_i\tilde{u}_j\right) + \frac{\partial}{\partial x_i}\overline{p} - \frac{\partial}{\partial x_j}\hat{\tau}_{ij} = -\frac{\partial}{\partial x_j}\tau_{ij}^{sgs} \tag{2.2}$$

$$\frac{\partial}{\partial t}\left(\overline{\rho}\hat{E}\right) + \frac{\partial}{\partial x_j}\left(\left(\overline{\rho}\hat{E} + \overline{p}\right)\tilde{u}_j\right) - \frac{\partial}{\partial x_j}\left(\tilde{u}_i\hat{\tau}_{ij}\right) + \frac{\partial}{\partial x_j}\hat{q}_j = -\frac{\partial}{\partial x_j}Q_j^{sgs} \tag{2.3}$$

where $\overline{\rho}$ and $\overline{p}$ are the filtered density and pressure, respectively. $\tilde{u}_i$ denotes the resolved Cartesian velocity component in the direction of the spatial Cartesian coordinate x_i and $\hat{E}$ is the resolved specific total energy per unit mass. The equations (2.1), (2.2), and (2.3) state the conservation of mass, momentum and energy, respectively. In these equations, the repeated indices indicate the Einstein summation convention. The pressure $\overline{p}$ in equation (2.2) is calculated from the equation of state as:

$$\overline{p} = (\gamma - 1)\left(\overline{\rho}\hat{E} - \frac{1}{2}\overline{\rho}\tilde{u}_i\tilde{u}_i\right) \tag{2.4}$$

where γ is the ratio of specific heats and it is 1.4 for air. $\hat{\tau}_{ij}$ in equations (2.2) and (2.3) represents the resolved viscous stress tensor. For a Newtonian fluid, it is calculated as:

$$\hat{\tau}_{ij} = \frac{\mu}{Re}\left(\frac{\partial \tilde{u}_i}{\partial x_j} + \frac{\partial \tilde{u}_j}{\partial x_i} - \frac{2}{3}\delta_{ij}\frac{\partial \tilde{u}_k}{\partial x_k}\right) \tag{2.5}$$

where μ refers to the fluid dynamic viscosity which can be obtained using Sutherland's law [28]. Re is the Reynolds number and δ_{ij} is the Kronecker delta.

$\hat{q}_j$ in equation (2.3) represents the resolved heat flux vector, which relates to the resolved total energy and velocity by

$$\hat{q}_j = \frac{\mu\gamma}{PrRe}\frac{\partial}{\partial x_j}\left(\hat{E} - \frac{1}{2}\tilde{u}_i\tilde{u}_i\right) \tag{2.6}$$

where Pr denotes the Prandtl number which is set to be 0.72.

Furthermore, equations (2.2) and (2.3) contain the subgrid scale terms, which show the effects of the unresolved subgrid scales. In these equations, τ_{ij}^{sgs} is the subgrid turbulent stress tensor and Q_j^{sgs} is the subgrid term in the filtered energy equation containing the turbulent stress term and the pressure-velocity term. They can be calculated as:

$$\tau_{ij}^{sgs} = \overline{\rho}\widetilde{u_i u_j} - \overline{\rho}\tilde{u}_i\tilde{u}_j \tag{2.7}$$

$$Q_j^{sgs} = \tau_{ij}^{sgs}\tilde{u_i} + \left(\overline{pu_j} - \overline{p}\tilde{u_j}\right)/\left(\gamma - 1\right) \tag{2.8}$$

These equations include the most dominant subgrid terms for the respective filtered momentum and energy equations. The closure of the filtered compressible Navier-Stokes equations needs these subgrid terms to be modeled. This is done as follows:

$$\tau_{ij}^{sgs} = -\mu_T\left(\frac{\partial\tilde{u}_i}{\partial x_j} + \frac{\partial\tilde{u}_j}{\partial x_i} - \frac{2}{3}\delta_{ij}\frac{\partial\tilde{u}_k}{\partial x_k}\right) \tag{2.9}$$

$$Q_j^{sgs} = \tilde{u_i}\tau_{ij}^{sgs} + \frac{\mu_T\gamma}{Pr_T}\frac{\partial}{\partial x_j}\left(\hat{E} - \frac{1}{2}\tilde{u}_i\tilde{u}_i\right) \tag{2.10}$$

where μ_T is the turbulent eddy viscosity and Pr_T is the turbulent Prandtl number which is set to be 0.9. Comparing equations (2.9) and (2.10) with equations (2.5) and (2.6) respectively, one can

see that they are modeled in essentially the same way. The differences are that molecular viscosity is replaced by turbulent viscosity (μ_T) and the Prandtl number is replaced by Pr_T (the turbulent Prandtl number). This modeling introduces μ_T, which needs to be calculated in order to close the system of equations. This closure is achieved using the WALE model, which is discussed in Section 2.2.

The filtered non-dimensional compressible Navier-Stokes equations can be rewritten in conservative form as follows. Note that the overbar symbols, showing the resolved quantities, have been omitted for simplicity:

$$\frac{\partial \mathbf{U}\left(\mathbf{x},t\right)}{\partial t} + \nabla \cdot \left[\mathbf{F}_e(\mathbf{U}) - \mathbf{F}_\nu(\mathbf{U}, \nabla \mathbf{U})\right] = 0 \tag{2.11}$$

Here $\mathbf{U}$ denotes the vector of resolved conservative flow variables, which can be written as:

$$\mathbf{U} = \left\{ \begin{array}{c} \overline{\rho} \\ \overline{\rho}\tilde{u_1} \\ \overline{\rho}\tilde{u_2} \\ \overline{\rho}\tilde{u_3} \\ \overline{\rho}\hat{E} \end{array} \right\} \tag{2.12}$$

The sub-script 1,2, and 3 refers to the streamwise, wall-normal, and spanwise direction, respectively.

$\mathbf{F}_e$ in equation (2.11) is the inviscid Cartesian flux vector that is represented by the resolved flow

variables and can be shown as:

$$\mathbf{F}_e^x = \left\{ \begin{array}{c} \overline{\rho}\tilde{u_1} \\ \overline{\rho}\tilde{u_1}^2 + \overline{p} \\ \overline{\rho}\tilde{u_1}\tilde{u_2} \\ \overline{\rho}\tilde{u_1}\tilde{u_3} \\ \left(\overline{\rho}\hat{E} + \overline{p}\right)\tilde{u_1} \end{array} \right\}, \quad \mathbf{F}_e^y = \left\{ \begin{array}{c} \overline{\rho}\tilde{u_2} \\ \overline{\rho}\tilde{u_1}\tilde{u_2} \\ \overline{\rho}\tilde{u_2}^2 + \overline{p} \\ \overline{\rho}\tilde{u_2}\tilde{u_3} \\ \left(\overline{\rho}\hat{E} + \overline{p}\right)\tilde{u_2} \end{array} \right\}, \quad \mathbf{F}_e^z = \left\{ \begin{array}{c} \overline{\rho}\tilde{u_3} \\ \overline{\rho}\tilde{u_1}\tilde{u_3} \\ \overline{\rho}\tilde{u_2}\tilde{u_3} \\ \overline{\rho}\tilde{u_3}^2 + \overline{p} \\ \left(\overline{\rho}\hat{E} + \overline{p}\right)\tilde{u_3} \end{array} \right\} \tag{2.13}$$

where the superscript x, y, and z here describe the components in the streamwise, wall-normal, and spanwise directions, respectively.

$\mathbf{F}_\nu$ in equation (2.11) represents the viscous Cartesian flux vector that combines the resolved viscous fluxes and the subgrid scale terms and this vector in each direction can be shown as:

$$\mathbf{F}_\nu^x = \left\{ \begin{array}{c} 0 \\ \hat{\tau}_{11} - \tau_{11}^{sgs} \\ \hat{\tau}_{12} - \tau_{12}^{sgs} \\ \hat{\tau}_{13} - \tau_{13}^{sgs} \\ \tilde{u_1}\hat{\tau}_{11} + \tilde{u_2}\hat{\tau}_{12} + \tilde{u_3}\hat{\tau}_{13} - \hat{q}_1 + Q_1^{sgs} \end{array} \right\} \tag{2.14}$$

$$\mathbf{F}_{\nu}^{y} = \begin{Bmatrix} 0 \\ \hat{\tau}_{12} - \tau_{12}^{sgs} \\ \hat{\tau}_{22} - \tau_{22}^{sgs} \\ \hat{\tau}_{23} - \tau_{23}^{sgs} \\ \tilde{u_1}\hat{\tau}_{12} + \tilde{u_2}\hat{\tau}_{22} + \tilde{u_3}\hat{\tau}_{23} - \hat{q}_2 + Q_2^{sgs} \end{Bmatrix} \tag{2.15}$$

$$\mathbf{F}_{\nu}^{z} = \begin{Bmatrix} 0 \\ \hat{\tau}_{13} - \tau_{13}^{sgs} \\ \hat{\tau}_{23} - \tau_{23}^{sgs} \\ \hat{\tau}_{33} - \tau_{33}^{sgs} \\ \tilde{u_1}\hat{\tau}_{13} + \tilde{u_2}\hat{\tau}_{23} + \tilde{u_3}\hat{\tau}_{33} - \hat{q}_{13} + Q_3^{sgs} \end{Bmatrix} \tag{2.16}$$

However, for the spatial discretization that will be performed in this work, the Cartesian viscous fluxes are rewritten as:

$$\mathbf{F}_{\nu}^{x} = \mathbf{G}_{1j}\frac{\partial \mathbf{U}}{\partial \mathbf{x}_j}, \quad \mathbf{F}_{\nu}^{y} = \mathbf{G}_{2j}\frac{\partial \mathbf{U}}{\partial \mathbf{x}_j}, \quad \mathbf{F}_{\nu}^{z} = \mathbf{G}_{3j}\frac{\partial \mathbf{U}}{\partial \mathbf{x}_j} \tag{2.17}$$

where the matrices $\mathbf{G}_{ij}(\mathbf{U})$ are determined by:

$$\mathbf{G}_{ij} = \frac{\partial \mathbf{F}_{\nu}^{x_i}}{\partial\left(\frac{\partial \mathbf{U}}{\partial \mathbf{x}_j}\right)} \tag{2.18}$$

for $i, j = 1, 2, 3$, so that they are only dependent on the resolved conservative flow variables. Further details on how these equations are used within the finite element formulation is provided in Chapter 3.

2.2 WALE Model

Large-eddy simulation techniques predict and analyze the instantaneous and statistical features of unsteady turbulent flows. The subgrid scale modeling is needed in order to account for the smaller scale motions. Specifically, μ_T in equations (2.9) and (2.10) needs to be modeled to close the system of equations as mentioned in the previous section. The subgrid scale modeling that is used in this work is the Wall-Adapting Local Eddy-viscosity (WALE) model. It was first proposed by Nicoud and Ducros [25] and is based on the square of the velocity gradient tensor.

In the WALE model, the turbulent eddy viscosity can be obtained as:

$$\mu_T = \rho \left(C_w \Delta\right)^2 \frac{\left(S_{ij}^d S_{ij}^d\right)^{3/2}}{\left(S_{ij} S_{ij}\right)^{5/2} + \left(S_{ij}^d S_{ij}^d\right)^{5/4}} \tag{2.19}$$

where C_w is a constant, which is assigned to be 0.5 in this work. The notation Δ is the local length scale of the element. The strain rate tensor for the resolved structures S_{ij} and the symmetric tensor S_{ij}^d in equation (2.19) are defined as:

$$S_{ij} = \frac{1}{2}\left(\frac{\partial \tilde{u}_i}{\partial x_j} + \frac{\partial \tilde{u}_j}{\partial x_i}\right) \tag{2.20}$$

$$S_{ij}^d = \frac{1}{2}\left(\frac{\partial \tilde{u}_i}{\partial x_k}\frac{\partial \tilde{u}_k}{\partial x_j} + \frac{\partial \tilde{u}_j}{\partial x_k}\frac{\partial \tilde{u}_k}{\partial x_i}\right) - \frac{1}{3}\delta_{ij}\frac{\partial \tilde{u}_l}{\partial x_k}\frac{\partial \tilde{u}_k}{\partial x_l} \tag{2.21}$$

where δ_{ij} is the Kronecker delta.

This method has a couple of advantages as pointed out in Ma et al. [29]: first, the spatial operator consists of a mixing of both the local strain and rotation rates; second, the eddy-viscosity

goes to zero naturally near the wall; third, the model produces zero eddy viscosity in case of pure shear. Furthermore, this model is invariant to coordinate translation or rotation and only local information is needed. These characteristics make it attractive for implementation in a parallel, finite element framework.

CHAPTER 3

NUMERICAL METHODS

The system of equations that were described in Chapter 2 are discretized both spatially and temporally. The Streamwise/Upwind Petrov-Galerkin (SUPG) method is used for the spatial discretization of the governing equations, while the second-order backward difference formula is used for time integration.

3.1 Streamwise/Upwind Petrov-Galerkin Discretization

The SUPG method modifies the standard Galerkin weighting functions by adding a streamline upwind perturbation to the formulation. In the SUPG method, the solution is assumed to be continuous across the computational domain, and a stabilization term is added to compensate for lack of dissipation.

The computational domain is divided into non-overlapping elements. The finite element approximation is expanded as a series involving the basis functions ϕ_i, and dependent variables $\hat{\mathbf{U}}_i$ for element k as:

$$\mathbf{U}^k = \sum_{i=1}^{npe} \hat{\mathbf{U}}_i^k \phi_i \left(\mathbf{x}\right) \tag{3.1}$$

where npe is the number of nodes per element. The summation is over all the nodes for element k. The set of basis functions is defined in a reference element spanning between $\{0 \leq \xi, \eta, \zeta \leq 1\}$,

where ξ, η, and ζ are the reference coordinates that correspond to x, y, and z in the physical coordinates, respectively. Therefore, a mapping from the reference to a physical element is required for the computation. The reference-to-physical transformation and the corresponding Jacobian J are given by:

$$\begin{aligned} x^k &= \sum_{i=1}^{npe} \hat{x}_i^k \phi_i(\xi, \eta, \zeta) \\ y^k &= \sum_{i=1}^{npe} \hat{y}_i^k \phi_i(\xi, \eta, \zeta) \\ z^k &= \sum_{i=1}^{npe} \hat{z}_i^k \phi_i(\xi, \eta, \zeta) \\ J &= \begin{bmatrix} \frac{\partial x}{\partial \xi} & \frac{\partial x}{\partial \eta} & \frac{\partial x}{\partial \zeta} \\ \frac{\partial y}{\partial \xi} & \frac{\partial y}{\partial \eta} & \frac{\partial y}{\partial \zeta} \\ \frac{\partial z}{\partial \xi} & \frac{\partial z}{\partial \eta} & \frac{\partial z}{\partial \zeta} \end{bmatrix} \end{aligned} \tag{3.2}$$

In the SUPG method, the governing equations (2.11) are multiplied by a weighting function and integrated over the domain Ω resulting in:

$$\begin{aligned} &\int_\Omega \phi \left[\frac{\partial \mathbf{U}}{\partial t} + \nabla \cdot (\mathbf{F}_e(\mathbf{U}) - \mathbf{F}_\nu(\mathbf{U}, \nabla \mathbf{U})) \right] d\Omega \\ &+ \sum_{k=1}^{nel} \int_{\Omega_k} \left[\left(\frac{\partial \phi}{\partial x} [\mathbf{A}] + \frac{\partial \phi}{\partial y} [\mathbf{B}] + \frac{\partial \phi}{\partial z} [\mathbf{C}] \right) \right] [\tau] \left[\frac{\partial \mathbf{U}}{\partial t} + \nabla \cdot (\mathbf{F}_e(\mathbf{U}) - \mathbf{F}_\nu(\mathbf{U}, \nabla \mathbf{U})) \right] d\Omega_k = 0 \end{aligned} \tag{3.3}$$

where nel is the number of elements and ϕ is a continuous weighting function defined over the domain. Note that the weighting function is the same as the basis functions for the dependent variables. The inviscid flux Jacobians [**A**],[**B**], and [**C**], and the stabilization matrix $[\tau]$ in the case

of inviscid flows are defined as:

$$[\mathbf{A}] = \left[\frac{\partial \mathbf{F}_e^x}{\partial \mathbf{U}}\right], \quad [\mathbf{B}] = \left[\frac{\partial \mathbf{F}_e^y}{\partial \mathbf{U}}\right], \quad [\mathbf{C}] = \left[\frac{\partial \mathbf{F}_e^z}{\partial \mathbf{U}}\right] \tag{3.4}$$

$$[\tau]^{-1} = \sum_j \left| \frac{\partial \phi_j}{\partial x}[\mathbf{A}] + \frac{\partial \phi_j}{\partial y}[\mathbf{B}] + \frac{\partial \phi_j}{\partial z}[\mathbf{C}] \right| \tag{3.5}$$

$$\left| \frac{\partial \phi_j}{\partial x}[\mathbf{A}] + \frac{\partial \phi_j}{\partial y}[\mathbf{B}] + \frac{\partial \phi_j}{\partial z}[\mathbf{C}] \right| = [\mathbf{T}][\Lambda][\mathbf{T}]^{-1} \tag{3.6}$$

where ϕ_j is the basis function associated with each node. [**T**] and [Λ] are the matrix of right eigenvectors and the diagonal matrix of eigenvalues of the left hand side of equation (3.6).

For viscous flows, additional terms are required as the Reynolds number decreases and the viscous terms become dominant. The derivation of the viscous contribution to the stabilization matrix is found in Erwin [30]. Using the equations (2.17) and (2.18) derived for the spatial discretization in Chapter 2, the viscous part of the stabilization matrix can be written as:

$$[\tau_\nu]^{-1} = \sum_j \left(\begin{bmatrix} \frac{\partial \phi_j}{\partial x} & \frac{\partial \phi_j}{\partial y} & \frac{\partial \phi_j}{\partial z} \end{bmatrix} \begin{bmatrix} G_{11} & G_{12} & G_{13} \\ G_{21} & G_{22} & G_{23} \\ G_{31} & G_{32} & G_{33} \end{bmatrix} \begin{bmatrix} \frac{\partial \phi_j}{\partial x} \\ \frac{\partial \phi_j}{\partial y} \\ \frac{\partial \phi_j}{\partial z} \end{bmatrix} \right) \tag{3.7}$$

In the SUPG method, the solution is assumed to be continuous over the computational domain. The stabilization matrix is added to compensate for lack of dissipation in the streamwise direction to prevent oscillations that occur for convection-dominated flows.

The volume integral in equation (3.3) is integrated by parts using the divergence theorem, which leads to:

$$\sum_{k=1}^{nel} \int_{\Omega_k} \phi \left[\frac{\partial \mathbf{U}}{\partial t} + \nabla \cdot (\mathbf{F}_e(\mathbf{U}) - \mathbf{F}_\nu(\mathbf{U}, \nabla \mathbf{U})) \right] d\Omega_k + \int_{\partial \Omega_k \cap \partial \Omega} \phi (\mathbf{F}_e(\mathbf{U}_b) - \mathbf{F}_\nu(\mathbf{U}_b, \nabla \mathbf{U})) dS$$
$$+ \sum_{k=1}^{nel} \int_{\Omega_k} \left[\left(\frac{\partial \phi}{\partial x} [\mathbf{A}] + \frac{\partial \phi}{\partial y} [\mathbf{B}] + \frac{\partial \phi}{\partial z} [\mathbf{C}] \right) \right] [\tau] \left[\frac{\partial \mathbf{U}}{\partial t} + \nabla \cdot (\mathbf{F}_e(\mathbf{U}) - \mathbf{F}_\nu(\mathbf{U}, \nabla \mathbf{U})) \right] d\Omega_k = 0 \tag{3.8}$$

Here, the subscript b refers to the boundary state. Note that the surface integrals in the SUPG method are computed only on the boundaries because of the continuity of the solution across the elements. Moreover, it implements a strong boundary enforcement at the wall, where the velocities and the turbulence variable are enforced to be zero.

3.2 Time-integration Scheme/Temporal Discretization

After discretization, equation (3.8) is re-written into the following differential equation form:

$$\mathbf{M} \frac{d\mathbf{U}}{dt} + \mathbf{R}(\mathbf{U}) = 0 \tag{3.9}$$

where **R** represents the discretized spatial residual including both inviscid and viscous terms. **M** is the mass matrix. In this work, a second-order backward difference formula (BDF2) is used for time integration. This can be written as:

$$\mathbf{R}^{n+1}(\mathbf{U}^{n+1}) = \frac{\mathbf{M}}{\Delta t} (\frac{3}{2} \mathbf{U}^{n+1} - 2\mathbf{U}^n + \frac{1}{2} \mathbf{U}^{n-1}) + \mathbf{R}(\mathbf{U}^{n+1}) = 0 \tag{3.10}$$

where $\mathbf{R}^{n+1}$ is the unsteady flow residual at time step $n+1$. For steady state problems, a local time-stepping method is used to reduce the stiffness of the system in the initial stages of calculation. This system in equation (3.10) is implicit, and it is solved using an approximate Newton method [31]. The approximate Newton method decomposes the flow Jacobian matrix with node-based diagonal and off-diagonal block components. The linearized system is solved using a preconditioned Generalized Minimal Residual (GMRES) method with ILU(k) preconditioning [32], [33]. The standard MPI message-passing library for inter-processor communication was used [34]. The mesh in this work is partitioned based on the METIS mesh partitioner [35].

The methods presented in this chapter are used to solve the governing equations numerically to investigate wall-pressure fluctuations in a turbulent boundary layer. However, spatially developing flows, such as turbulent boundary layers, pose a challenge in simulation. The flow downstream is highly dependent on the conditions at the inlet of the computational domain, making it necessary to specify time-dependent turbulent inflow conditions at the upstream boundary. The technique used for this is discussed in Chapter 4.

CHAPTER 4

INFLOW TURBULENCE GENERATION

Numerical simulations of fully developed, time-evolving flows, such as channel flow, are typically performed using periodic boundary conditions in the streamwise direction. For this case, the downstream flow is directly re-applied at the inlet of the domain. However, in the case of spatially developing flows, these boundary conditions are not appropriate. The flow downstream is significantly influenced by the flow characteristics upstream in the computational domain. Therefore incorrect flow information at the inlet will result in an inaccurate downstream flow simulation. Therefore, a technique to reconstruct unsteady turbulent fluctuating velocity components at the inlet boundary is required. The ideal turbulent inflow boundary condition needs to have the appropriate turbulence structures while simultaneously satisfying the Navier-Stokes equations.

4.1 Introduction

The most straightforward approach to generate realistic time series of turbulent fluctuations that are in equilibrium with the mean flow is to use a computational domain with a very long length in the streamwise direction and start the calculation using a laminar profile with random distribution at the inlet of the domain [36]. This approach is very costly as one has to wait for a natural transition to turbulence to occur. Furthermore, re-laminarization may take place instead of transitioning to

turbulence in a lot of cases. In an effort to reduce computational simulation time, various methods for inflow generation have been proposed.

Techniques can basically be classified into: (1) synthetic methods, and (2) recycling and rescaling methods [37]. Some of the reviews of these methods specifically using large-eddy simulation can be found in [38], [39], and [40]. The fundamental idea behind the synthetic methods is to take a mean velocity profile and superimpose random fluctuations to generate turbulent inflow velocity information. A significant body of literature about the synthetic methods can be found, which include white-noise random fluctuations [41], Fourier techniques [42], digital filter approach [43], proper orthogonal decomposition method [44], and vortex method and synthetic eddy method [39, 45]. Xiao et al. mentioned in [37] that there are two drawbacks in the synthetic turbulence generation approaches. First of all, the adjustment region of the development of turbulence structures is always present to some extent. For example, Lund et al. [46] pointed out that a development region of approximately 50 boundary layer thickness was required for a wall boundary layer. Secondly, turbulence information needed for these approaches, for example turbulent length scales or correlation shapes, is rarely available for input.

These problems can be avoided by using the recycling and rescaling method presented in this work. The basic idea for the recycling and rescaling methods is to "recycle" the turbulent velocity profile from a specific plane within the computational domain, "rescale" it properly, and re-introduce it at the inlet of the domain as the inflow boundary conditions of the computational domain. This is depicted in Figure 4.1 for the flat plate boundary layer in two-dimensional case.

First a brief review of the basic recycling and rescaling method is provided. Then the specific method used in this work is presented.

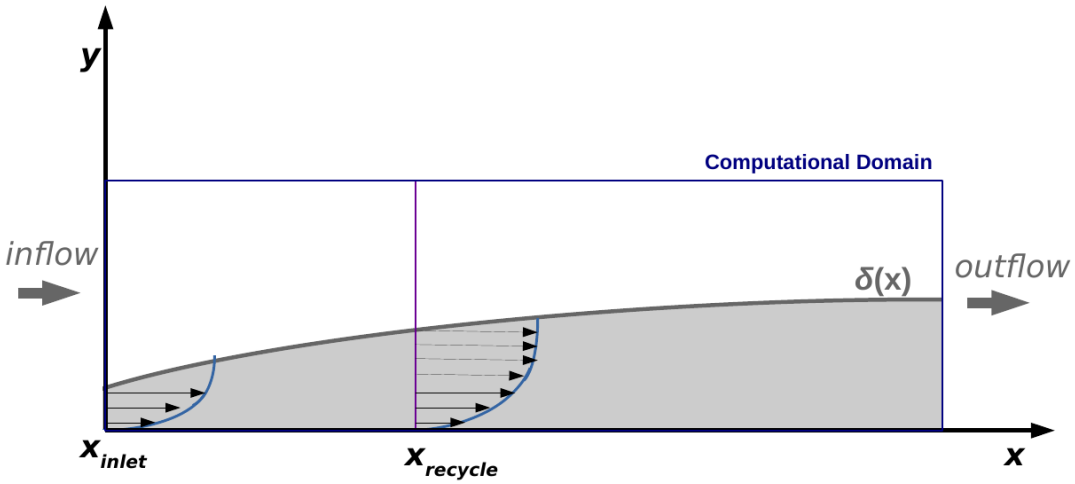

Figure 4.1 Illustration of the flat plate boundary layer in two-dimensional domain

4.2 Literature Review of Recycling and Rescaling Method

The most popular and fundamental recycling and rescaling method is the one developed by Lund et al. [46] who simplified the method originally proposed by Spalart and Leonard [47]. Spalart and Leonard noticed that unlike fully-developed channel flow, for example, boundary layers are not homogeneous in the streamwise direction, which makes periodic conditions not applicable a priori. They introduced a set of coordinate lines, so that the streamwise inhomogeneity associated with the boundary layer growth is minimized when the Navier-Stokes equations are transformed into this coordinate system. The periodic boundary conditions can then be used in this case in the streamwise direction. Lund et al. noticed that the method by Spalart and Leonard [47] produced the most accurate inflow condition but the computation was somewhat complicated. This motivated them to make modifications to the method by Spalart and Leonard [47] and make it simpler to program.

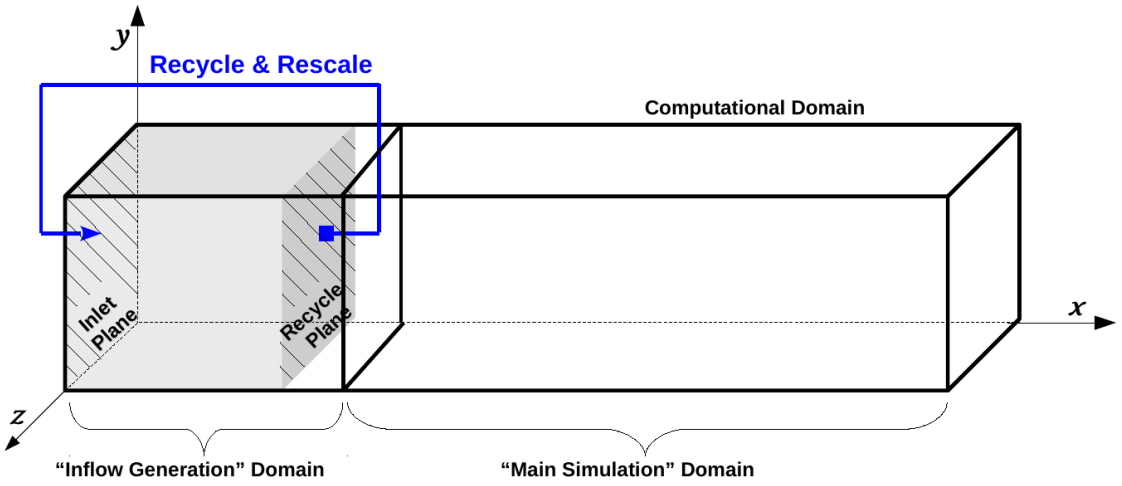

Figure 4.2 Illustration of the basic recycle and rescale process by Lund et al. [46]

Lund et al. [46] proposed a simple yet powerful method to estimate the velocity at the inlet of the domain. They divided the computational domain into the inflow generation domain and the main simulation domain. The velocity profile at the inlet plane is based on the solution downstream of the inflow generation domain, specifically from the recycle plane. They extracted the velocity field from the recycle plane, which is a plane near the exit of the inflow generation domain, made use of the ideas of Spalart and Leonard [47] to rescale it, and then reintroduced it as a boundary condition at the inlet of the computational domain. This is illustrated in Figure 4.2. This method is simple in that it does not require coordinate frame transformation as required by Spalart and Leonard [47].

The method proposed by Lund et al. [46] is the basic method used in this work. In this method, the velocity is first decomposed into a mean and fluctuating part as:

$$u_i(x,y,z,t) = U_i(x,y) + u_i'(x,y,z,t) \tag{4.1}$$

where u_i is the instantaneous velocity in the i^{th} direction, and $i = 1, 2, 3$. The streamwise, wall-normal, and spanwise directions are x, y, and z directions, respectively, and the velocity components in the x, y, and z directions as u, v, and w, respectively. In this case, $u_1 = u$, $u_2 = v$, and $u_3 = w$ in equation (4.1). In the same way, $u_i^{'}$ represents the velocity fluctuations in the i^{th} direction, and U_i denotes the mean velocity as an average in the spanwise direction and in time. The motivation behind decomposing the velocity is to apply different scalings to the mean and fluctuating components.

The mean streamwise velocity is rescaled according to the law of the wall in the inner region [48] and the defect law in the outer region [49]. The mean vertical velocity is scaled approximately, since V itself is a small quantity. The fluctuations are decomposed to isolate the streamwise inhomogeneity through the dependence on the friction velocity u_τ.

The overall rescaling for each component is computed as following:

$$U_{inlet}^{inner} = \gamma U_{recycle}\left(y_{inlet}^{+}\right) \tag{4.2}$$

$$U_{inlet}^{outer} = \gamma U_{recycle}\left(\eta_{inlet}\right) + \left(1-\gamma\right) U_{\infty} \tag{4.3}$$

$$V_{inlet}^{inner} = V_{recycle}\left(y_{inlet}^{+}\right) \tag{4.4}$$

$$V_{inlet}^{outer} = V_{recycle}\left(\eta_{inlet}\right) \tag{4.5}$$

$$\left(u_i^{'}\right)_{inlet}^{inner} = \gamma\left(u_i^{'}\right)_{recycle}\left(y_{inlet}^{+}, z, t\right) \tag{4.6}$$

$$\left(u_i^{'}\right)_{inlet}^{outer} = \gamma\left(u_i^{'}\right)_{recycle}\left(\eta_{inlet}, z, t\right) \tag{4.7}$$

where y^+ is the inner coordinate, which is defined as:

$$y^+ = \frac{(u_\tau y)}{\nu} \tag{4.8}$$

where ν is the kinematic viscosity and u_τ is the friction velocity which is calculated as:

$$u_\tau = \sqrt{\nu \left(\frac{\partial U}{\partial y}\right)_{wall}} \tag{4.9}$$

The friction velocity is a unique scaling parameter for the inner and outer quantities. η is the outer coordinate, which is expressed as:

$$\eta = \frac{y}{\delta} \tag{4.10}$$

where δ is the boundary layer thickness. U_∞ in equation (4.3) is the freestream velocity, and γ in equations (4.2), (4.3), (4.6), and (4.7) is the scaling factor (not the ratio of specific heat) which is calculated as:

$$\gamma = \left(\frac{u_{\tau,inlet}}{u_{\tau,recycle}}\right) \tag{4.11}$$

In these equations, U_{inlet}^{inner}, for example, means the average velocity at the inlet plane in the inner region of the boundary layer. y_{inlet}^+ indicates the y inner coordinate at the inlet plane. Moreover, $U_{recycle}\left(y_{inlet}^+\right)$ is the mean velocity at the recycle plane, expressed as a function of y^+ and evaluated at the inner coordinate of the mesh at the inlet plane. A linear interpolation is needed to evaluate this, as the inner coordinate of the mesh at the inlet and the recycle planes are different in general. For the rescaling part of this method, both u_τ and δ need to be known at the inlet

and recycle planes. At the recycle plane, these can be determined from the mean velocity profile. However, for the inlet plane, they need to be specified. Here, only δ_{inlet} needs to be specified as $u_{\tau,inlet}$ can be calculated by:

$$u_{\tau,inlet} = u_{\tau,recycle}\left(\frac{\theta_{recycle}}{\theta_{inlet}}\right)^{\frac{1}{8}} \tag{4.12}$$

where θ is the momentum thickness for incompressible flow, defined as:

$$\theta = \int_0^\infty \frac{U}{U_\infty}\left(1 - \frac{U}{U_\infty}\right) dy \tag{4.13}$$

The composite velocity equation for each point in the inlet plane proposed by Lund et al. [46] can then be shown as:

$$(u_i)_{inlet} = \left[(U_i)_{inlet}^{inner} + \left(u_i^{'}\right)_{inlet}^{inner}\right]\left[1 - W\left(\eta_{inlet}\right)\right] + \left[(U_i)_{inlet}^{outer} + \left(u_i^{'}\right)_{inlet}^{outer}\right]\left[W\left(\eta_{inlet}\right)\right] \tag{4.14}$$

where W is a weighting function and is calculated as:

$$W(\eta) = \frac{1}{2}\left\{1 + \frac{tanh\left[\frac{\alpha(\eta-b)}{(1-2b)\eta+b}\right]}{tanh(\alpha)}\right\} \tag{4.15}$$

where $\alpha = 4$ and $b = 0.2$. The weighting function is 0 at η=0, 0.5 at η=b, and 1 at η=1. The parameter α controls the width of the region over which the function transitions from 0 to 1. The values of α and b are chosen through analysis of an independent spatially evolving boundary layer simulation performed by Lund et al. [46].

Lund et al. [46] applied this method to generate turbulent inflow boundary conditions for the main simulation and successfully solved the incompressible Navier-Stokes equations using large-eddy simulations. However, a number of studies [50–55] have shown drawbacks of this technique, including spurious periodicity, error accumulation, and initial conditions that make the method difficult to implement. Further details on these hurdles and the methods developed to overcome these difficulties are presented in the next section.

4.3 Modified Recycling and Rescaling Method

The inflow turbulence generation method used in this work is based on and the modification to the work of Arolla et al. [56]. Arolla et al. introduced and validated one of the many variants of the recycling and rescaling method for the large eddy simulation of turbomachinery flows. They have adopted the method proposed by Spalart et al. [57], who simplified the recycling procedure derived from that of Lund et al. [46].The modifications include: (1) applying one scaling throughout the wall-normal direction, since the near-wall turbulence regenerates itself much faster than the outer one, (2) using a short recycling distance to reduce the computing cost, and (3) omitting the effect of the vertical velocity component which has been observed to have minimal effects. These modifications make the recycling and rescaling process much easier than the one used by Lund et al. [46] as single scaling is applied, and there is no need to decompose the velocity component. Arolla et al. [56] have also used the mirroring method proposed by Jewkes et al. [58] to avoid the spurious linking of spanwise structures and the accompanying error accumulation. The details of these operations are shown later in this chapter.

The main differences between their method [56] and the present work are the initialization and the fact that the mean streamwise velocity is kept fixed at the inlet plane. The overall algorithm that is used in this work is explained in detail next.

4.3.1 Initial Conditions

The initial conditions used in the work of Lund et al. [46] is to initialize the velocity field with the mean profile given by the Spalding's law of the wall [5] and superimpose random fluctuations with a maximum amplitude of 10% of the free-stream velocity. However, one of the main issues of the recycling and rescaling method proposed by Lund et al. [46], that is pointed out in the literature [56, 58, 59], is about the effect of the initialization. If the initialization is not carefully implemented, the friction velocity or Reynolds stresses decreases continually and the flow may become laminar. Keeping the friction velocity from continually decreasing can be quite challenging in implementing the inflow generation method. Different modifications to the initial conditions of Lund et al. [46] have been proposed to overcome this issue.

Bohr et al. [60] initialized the flow field using the $\frac{1}{7}$ power law and random fluctuations, and successfully maintained the friction velocity at the target value. Liu and Pletcher [54] noticed that the skin friction may decrease with time if the recycling starts by using downstream data that are far from a correct turbulent state. The difficulty of achieving the desired inflow turbulent state results from coupling of the initial and inflow condition during the starting transient. As the initial condition influences the length of the starting transient, Liu and Pletcher [54] devised a method to dynamically position the recycling plane according to the downstream instantaneous field, still using the random fluctuations to generate the initial fluctuation field.

In the same manner, Araya et al. [61] added an additional plane, called the test plane, located between the inlet and recycle planes, and used different velocity scales for the inner and outer regions. They tested their method in zero, favorable, and adverse pressure gradient flows. For the initialization, they used a linear profile close to the wall and the $\frac{1}{7}$ power law far from the wall with some random fluctuations of a maximum amplitude of 10% of the free-stream velocity.

Jewkes et al. [58] used a simple mean profile provided by the Spalding's law of the wall [5] and initialized velocity fluctuation intensities to roughly match intensity profiles in the boundary layer. Arolla et al. [56] also initialized the mean flow using Spalding's law of the wall and the fluctuations in a way that the maximum is around $\frac{y}{\delta} = 0.05$ and progressively die away towards the outer layer.

The initialization used in this work is the same as that of Jewkes et al. [58], wherein the mean velocity profile is taken from the Spalding's law of the wall and the fluctuations match the desired intensity profiles.

The mean velocity for initial conditions is calculated from Spalding's composite law of the wall as:

$$y^+ = u^+ + e^{-\kappa B}\left[e^{\kappa u^+} - 1 - \kappa u^+ - \frac{(\kappa u^+)^2}{2} - \frac{(\kappa u^+)^3}{6}\right] \tag{4.16}$$

where κ is chosen to be 0.41 and B is 5.0. This is shown in Figure 4.3a, which is in terms of u^+ vs y^+. It needs to be expressed in terms of u vs y to be used directly in the simulation as initial conditions.

Using equation (4.8) and the following:

$$u^+ = \frac{u}{u_\tau} \tag{4.17}$$

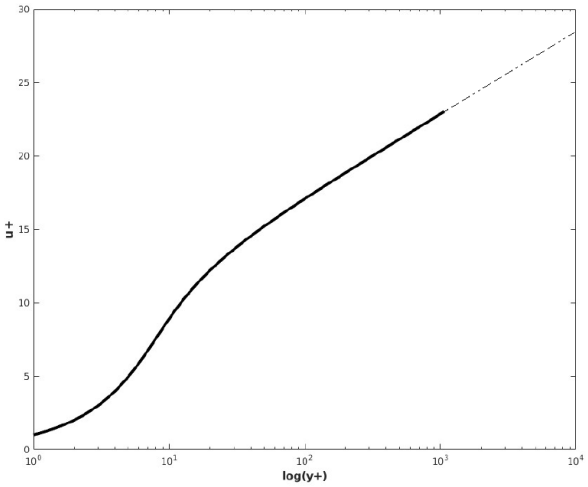

(a) As a function of u^+ vs y^+

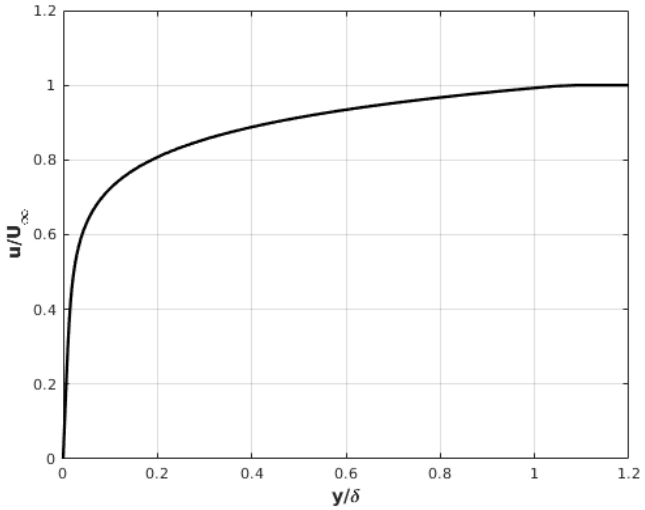

(b) As a function of u/U_∞ vs y/δ

Figure 4.3 Spalding profile generated for the initial conditions

equation (4.16) can be rewritten in terms of u vs y/δ. This is depicted in Figure 4.3b.

The velocity fluctuations are randomly chosen from the range set as:

$$\begin{aligned} |u'| \leq 0.8u, \;\; |v'| \leq 0.5v, \;\; |w'| \leq 0.6w \qquad for \;\; 0.05 \leq \frac{y}{\delta} < 0.25 \\ |u'| \leq 0.4u, \;\; |v'| \leq 0.25v, \;\; |w'| \leq 0.3w \qquad for \;\; 0.25 \leq \frac{y}{\delta} < 0.5 \\ |u'| \leq 0.2u, \;\; |v'| \leq 0.125v, \;\; |w'| \leq 0.15w \qquad for \;\; 0.5 \leq \frac{y}{\delta} \leq 1 \end{aligned} \tag{4.18}$$

where the amplitude is set for the range of $0.05 \leq \frac{y}{\delta} < 0.25$, and is reduced by a factor of two in the region $0.25 \leq \frac{y}{\delta} < 0.5$ and by a factor of four in the region $0.5 \leq \frac{y}{\delta} \leq 1$. The initial fluctuations are zero when $y > \delta$.

The initial velocity field contour in the x-y plane of the computational domain is presented in Figure 4.4. This velocity field is composed of the mean value from the Spalding's composite law of the wall and the fluctuations shown in equation (4.18) above. The values of x and y are in meters. As can be seen from the figure, δ = 0.1m was chosen and the intensity is zero beyond $y = \delta$.

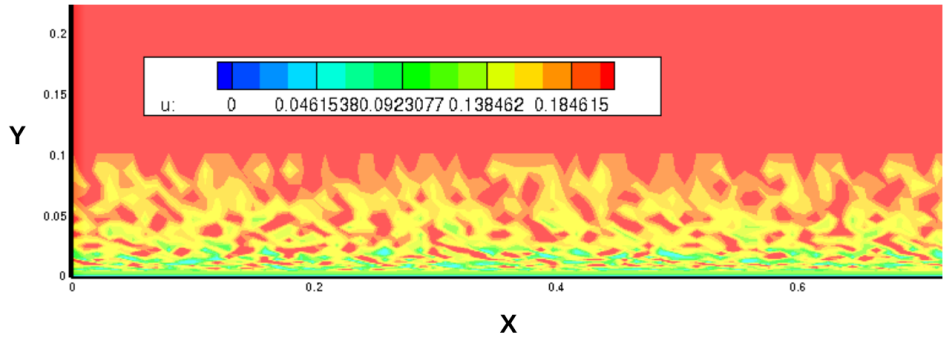

Figure 4.4 Streamwise velocity initial conditions in x-y plane

4.3.2 Proposed Recycling and Rescaling Method

In the work of Arolla et al. [56], a single scaling is applied throughout and therefore no decomposition of the velocity field is required. The streamwise velocity component at the inlet is computed as:

$$u(x,y,z,t)_{inlet} = u\left(x, y\left(\frac{\delta_{recycle}}{\delta_{inlet}}\right), z, t\right)_{recycle} \tag{4.19}$$

y is a function of $\left(\frac{\delta_{recycle}}{\delta_{inlet}}\right)$ in equation (4.19); this arises from the similarity relationship, $\eta_{inlet} = \eta_{recycle}$. In practical terms, for each point in the inlet plane, the rescaled value comes from the corresponding point in the recycle plane with the outer scaling applied. One can draw the mapping equation from the point in the inlet plane to the point in the recycle plane where the rescaled values are extracted from:

$$y_{recycle} = \frac{\delta_{recycle}}{\delta_{inlet}} y_{inlet} \tag{4.20}$$

This is illustrated in Figure 4.5.

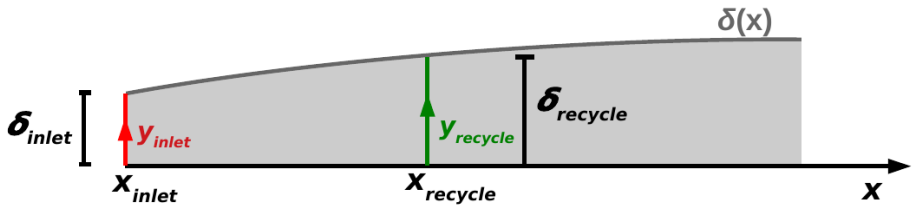

Figure 4.5 Illustration of the mapping from the point in the inlet plane to the point in the recycle plane

Using this recycling and rescaling method, the friction velocity decreases initially to $0.036U_\infty$, increases after that and eventually reaches a stable value of $0.043U_\infty$ after about 100 inertial time scales (TU_∞/δ) [56]. However, if the mean streamwise velocity at the inlet is kept fixed throughout the simulation domain, the friction velocity does not decrease as much and achieves the target value of about $0.046U_\infty$ easily (details in Chapter 6). Therefore, the mean streamwise velocity is fixed at the inlet in this work. It is computed in the same way as in the initial conditions by Spalding's law of the wall [5], noted as $U_{Spalding}\left(x_{inlet}, y\right)$ in equation (4.21) below. In this case, the single scaling is applied to the streamwise velocity fluctuations instead of the velocity itself.

Therefore, the mean streamwise velocity at the inlet plane is calculated as:

$$u\left(x,y,z,t\right)_{inlet} = U_{Spalding}\left(x_{inlet}, y\right) + u^{'}\left(x,y,z,t\right)_{inlet} \tag{4.21}$$

where streamwise velocity fluctuations at the inlet are calculated from those at the recycle plane as:

$$u^{'}(x,y,z,t)_{inlet} = u^{'}\left(x, y\left(\frac{\delta_{recycle}}{\delta_{inlet}}\right), z, t\right)_{recycle} \tag{4.22}$$

The streamwise fluctuations at the recycle plane on the right-hand-side is computed by subtracting the average streamwise velocity from the instantaneous velocity,

$$u^{'}\left(x,y,z,t\right)_{recycle} = u\left(x,y,z,t\right)_{recycle} - U\left(x,y\right)_{recycle} \tag{4.23}$$

where $U\left(x,y\right)_{recycle}$ is obtained by averaging the velocity $u\left(x,y,z,t\right)_{recycle}$ over the time period and over the spanwise direction. The evaluation shown in equation (4.22) requires an interpolation,

since the value of $y\left(\frac{\delta_{recycle}}{\delta_{inlet}}\right)$ for the grid nodes at the recycle and inlet stations are different in general. A linear interpolation has been found to be sufficiently accurate. Since one scaling is used for the rescaling part, no weight function needs to be specified.

The wall normal velocity component v is omitted in this recycling and rescaling method, because the corrections to it have very little effect. The spanwise velocity component w should be zero in the mean, so no scaling is needed.

The location of the recycling plane has to be specified in the recycling and rescaling process. Additionally, the mirroring method is implemented in the proposed method. These are explained next.

4.3.3 Recycling Distance and Mirroring Method

The recycling and rescaling process starts from the recycle plane. Therefore, a shorter recycling distance will reduce the computational cost [57]. However, if the distance becomes too short, no natural evolution of the eddies will take place. There is potential for numerical artifacts to be introduced to the mean flow, if the inflow and recycle planes are located close to one another [58, 62, 63]. The location of the recycle plane varies in the literature. Lund et al. [46] placed the recycle plane at $8.25\delta_0$ downstream of the inlet, where δ_0 is the 99% boundary layer thickness at the midpoint of the inflow generation domain. The location used in the current work is chosen to be $2.5\delta_{inlet}$ from the inlet plane, which is about 25% of the streamwise length of the domain.

In order to deal with the spurious feedback behavior caused by placing the recycle plane close to the inlet, a mirroring technique was used in Jewkes et al. [58]. It was applied from the

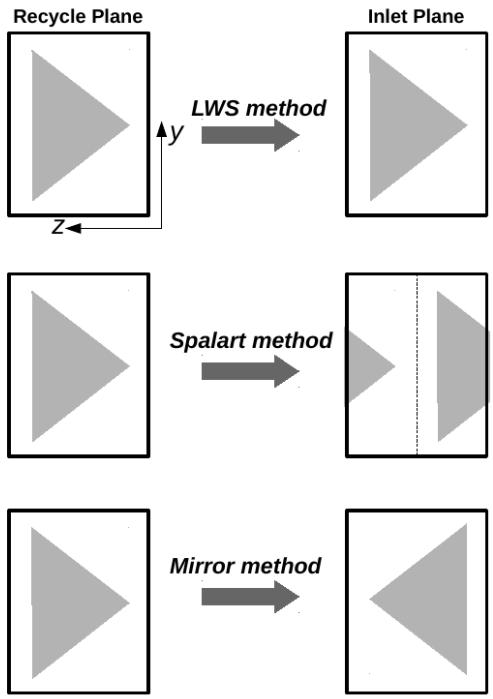

Figure 4.6 Illustration of the mirroring method from Jewkes et al. [58]

rescaled inlet velocity field as:

$$\begin{aligned} u(y,z,t)_{mirror,inlet} &= u(y,W-z,t)_{inlet} \\ v(y,z,t)_{mirror,inlet} &= v(y,W-z,t)_{inlet} \\ w(y,z,t)_{mirror,inlet} &= -w(y,W-z,t)_{inlet} \end{aligned} \tag{4.24}$$

where W is the domain width in the spanwise direction and t is the time. This method is designed to avoid spurious linking between inlet and recycle planes by removing any streamwise alignment, while maintaining the realistic coherent structures at the inlet. This is compared to the methods of Lund et al. [46] and Spalart et al. in [58] and is illustrated in Figure 4.6.

The modified recycling and rescaling method along with the mirroring method is illustrated in Figure 4.7. The mirroring method is shown as the flipped lightning bolt to demonstrate equation (4.24) and Figure 4.6.

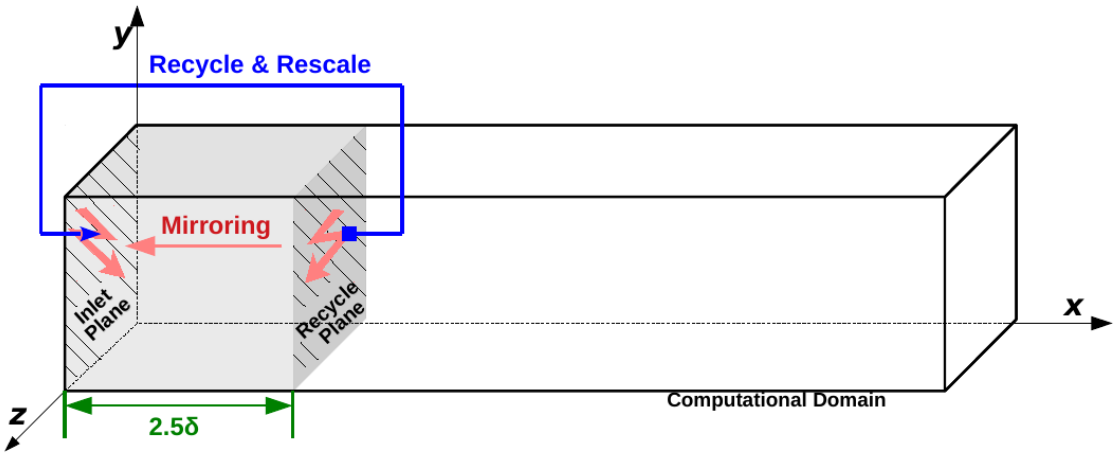

Figure 4.7 Illustration of the modified inflow turbulent generation method

4.3.4 Boundary Conditions and Sponge Layer

Now that the inflow conditions have been specified, boundary conditions on other surfaces need to be identified. Consider Figure 4.8 which shows the boundary conditions in the computational domain.

The plate at the bottom has the "no-slip" boundary condition of the viscous flow. The periodic boundary conditions are applied to the two sides of the domain in the z-direction, in a way that the solution $\frac{d\mathbf{U}}{dt}$ in equation (3.9) is the same on both sides of the domain [64]. One of the sides is called the "primary" plane, and the other the "secondary" plane. These definitions are arbitrary and can be interchanged. This is illustrated in Figure 4.9.

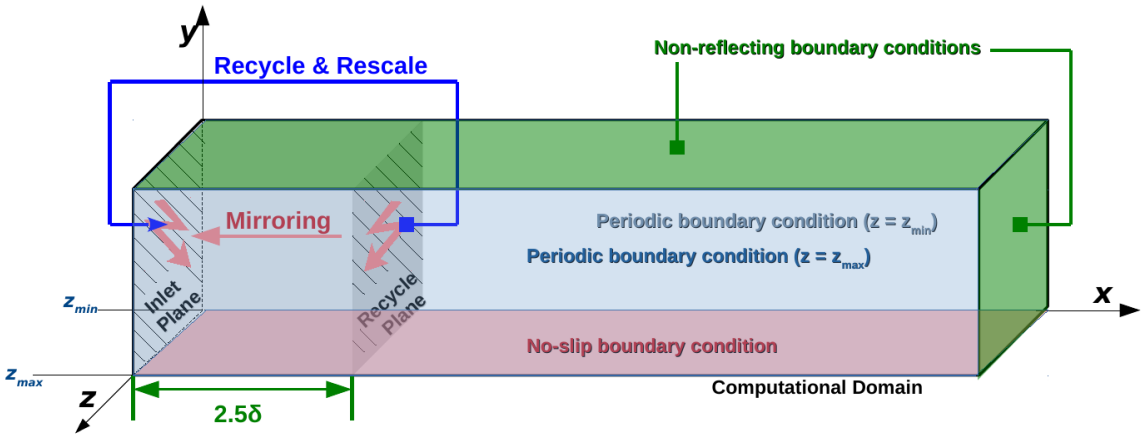

Figure 4.8 Illustration of the various boundary conditions in the computational domain

To illustrate the point, assume that there are three planes: primary, interior, and secondary, as shown in Figure 4.9. Then equation (3.9) can be rewritten as:

$$\begin{bmatrix} \mathbf{M}_{SS} & \mathbf{M}_{SI} & \mathbf{M}_{SP} \\ \mathbf{M}_{IS} & \mathbf{M}_{II} & \mathbf{M}_{IP} \\ \mathbf{M}_{PS} & \mathbf{M}_{PI} & \mathbf{M}_{PP} \end{bmatrix} \begin{bmatrix} \mathbf{x}_S \\ \mathbf{x}_I \\ \mathbf{x}_P \end{bmatrix} = \begin{bmatrix} \mathbf{R}_S \\ \mathbf{R}_I \\ \mathbf{R}_P \end{bmatrix} \tag{4.25}$$

where P, S, and I denote the primary, secondary, and interior planes, respectively. $\mathbf{x}$ is $\frac{d\mathbf{U}}{dt}$ in equation (3.9). Imposing the periodic boundary condition gives $\mathbf{x}_S = \mathbf{x}_P$, which results in:

$$\begin{bmatrix} \mathbf{I} & \mathbf{0} & -\mathbf{I} \\ \mathbf{M}_{IS} & \mathbf{M}_{II} & \mathbf{M}_{IP} \\ \mathbf{M}_{PS} + \mathbf{M}_{SS} & \mathbf{M}_{PI} + \mathbf{M}_{SI} & \mathbf{M}_{PP} + \mathbf{M}_{SP} \end{bmatrix} \begin{bmatrix} \mathbf{x}_S \\ \mathbf{x}_I \\ \mathbf{x}_P \end{bmatrix} = \begin{bmatrix} \mathbf{0} \\ \mathbf{R}_I \\ \mathbf{R}_P + \mathbf{R}_S \end{bmatrix} \tag{4.26}$$

where $\mathbf{I}$ is the identity matrix and $\mathbf{0}$ is the null matrix.

Eliminating the first row results in:

$$\begin{bmatrix} \mathbf{M}_{II} & \mathbf{M}_{IP} + \mathbf{M}_{IS} \\ \mathbf{M}_{PI} + \mathbf{M}_{SI} & \mathbf{M}_{PP} + \mathbf{M}_{SP} + \mathbf{M}_{PS} + \mathbf{M}_{SS} \end{bmatrix} \begin{bmatrix} \mathbf{x}_I \\ \mathbf{x}_P \end{bmatrix} = \begin{bmatrix} \mathbf{R}_I \\ \mathbf{R}_P + \mathbf{R}_S \end{bmatrix} \tag{4.27}$$

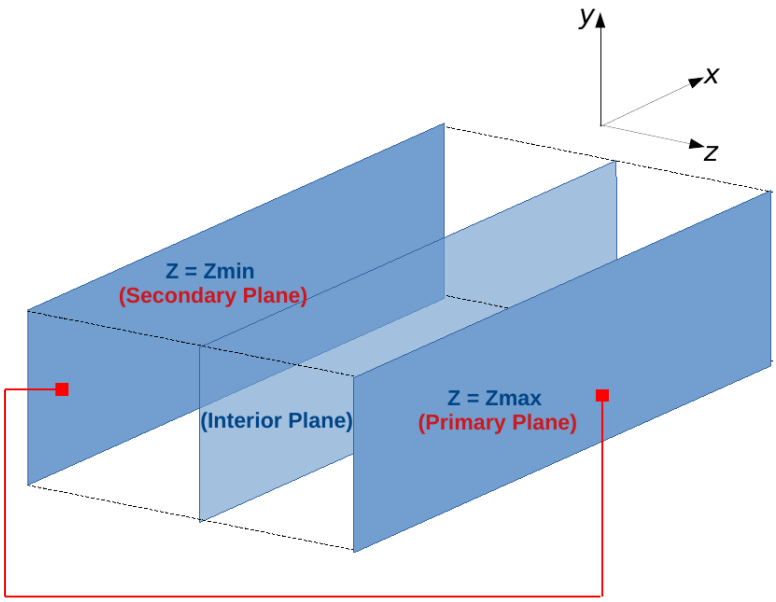

Figure 4.9 Illustration of the periodic boundary conditions with the primary and secondary planes in the computational domain

The top and exit surfaces of the computational domain can simply be specified as the far-field boundary conditions. However, this can result in unwanted reflections at the boundary. In order to overcome this problem, the so-called non-reflecting boundary conditions need to be applied. In the present work, they are implemented using a "sponge layer" [65]. The sponge layer is a layer of cells wherein a source term is applied. This source term causes any fluctuations that

are headed to the boundary to decay thereby minimizing any reflections back in the computational domain. This is taken to have the size of about δ_{inlet} from the top and exit boundaries in this work, and is illustrated in Figure 4.10.

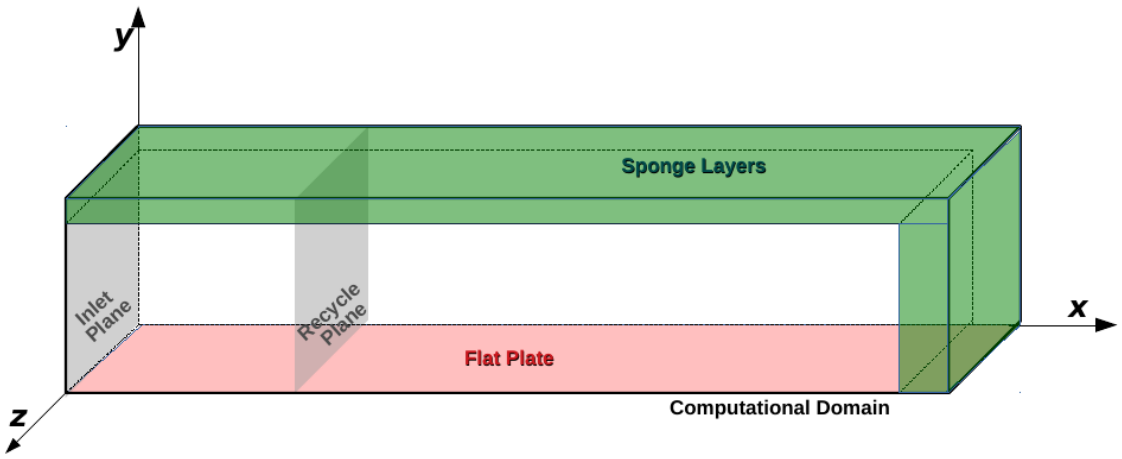

Figure 4.10 Illustration of the sponge layers (in green) at the top and exit boundaries in the computational domain

The source terms S in the sponge layer for the upper surface boundary conditions are evaluated as a function of the deviation of the instantaneous variables Q, i.e., ρ, u, v, w, T, and the freestream values Q_∞:

$$S = \sigma\left(y\right)\left(Q(y_{node}) - Q_\infty\right) \tag{4.28}$$

For the exit boundary conditions, the source terms in the sponge layer are calculated as a function of the difference between the instantaneous variables Q and those evaluated at the recycle plane $Q_{recycle}$:

$$S = \sigma\left(x\right)\left(Q(x_{node}) - Q_{recycle}\right) \tag{4.29}$$

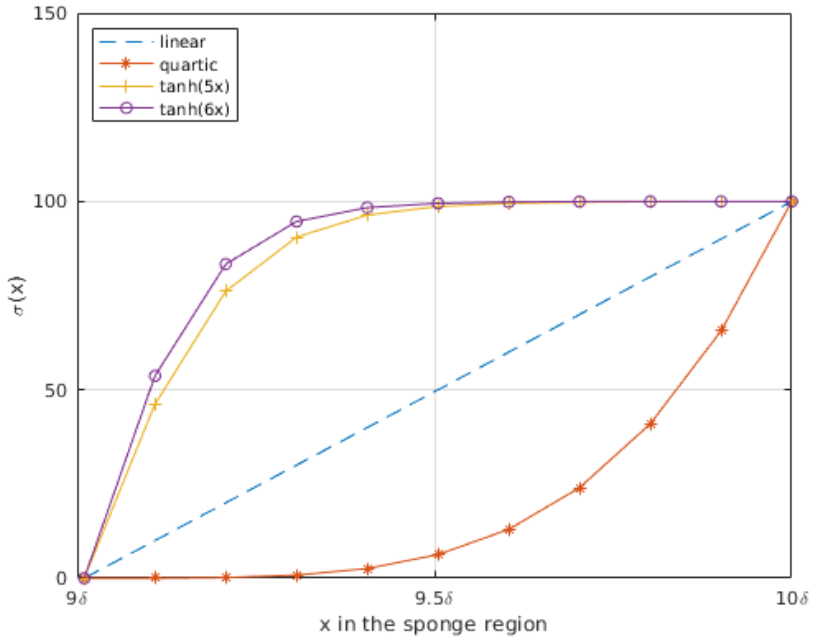

Figure 4.11 Examples of different types of $\sigma(x)$ in the sponge layer in the x direction with $\sigma_{max} = 100$

In equations (4.28) and (4.29), $\sigma(x)$ and $\sigma(y)$ are computed such that it increases from 0 to σ_{max} within the sponge layer, where σ_{max} is taken to be 100 in this work. Examples of different types of variations of $\sigma(x)$ are presented in Figure 4.11.

In order for the sponge layer to be effective as soon as it starts, $tanh(6x)$ is used in this work. In this case, the equations for $\sigma(x)$ and $\sigma(y)$ can be written as:

$$\begin{aligned} \sigma(x) &= tanh\left[6\left(\frac{x_{node} - x_{sponge}}{L_x - x_{sponge}}\right)\right]\sigma_{max}, \\ \sigma(y) &= tanh\left[6\left(\frac{y_{node} - y_{sponge}}{L_y - y_{sponge}}\right)\right]\sigma_{max}, \end{aligned} \tag{4.30}$$

where L_x and L_y are the domain length in the streamwise and wall-normal directions, respectively. Also, x_{sponge} and y_{sponge} denote the starting location of the sponge layer in the streamwise and wall-normal directions, respectively.

CHAPTER 5

STATISTICS

Turbulent flow is characterized by significant unsteadiness of the various flow variables. One way to understand their macroscopic behavior is to look at the statistics of the turbulent flow. These statistics could be as simple as the averages or can be as complicated as multi-point correlations. A brief background on the statistics employed in the current study is presented here.

5.1 Reynolds Stress Tensor Components

First of all, the Reynolds stress tensor components, ${u'}_{rms}$, ${v'}_{rms}$, ${w'}_{rms}$, and $u'v'$, are computed. These data are normalized by the local friction velocity u_τ as:

$$\begin{aligned} {u'}_{rms} &= \frac{\sqrt{\overline{u'^2}}}{u_\tau}, \\ {v'}_{rms} &= \frac{\sqrt{\overline{v'^2}}}{u_\tau}, \\ {w'}_{rms} &= \frac{\sqrt{\overline{w'^2}}}{u_\tau}, \\ u'v' &= \frac{\overline{u'v'}}{u_\tau^2}, \end{aligned} \tag{5.1}$$

where $\overline{u'^2}$ is computed as:

$$\overline{u'^2} = \overline{(u-\overline{u})(u-\overline{u})} = \overline{u^2 - 2u\overline{u} - \overline{u}^2} = \overline{u^2} - 2\overline{u}\,\overline{u} + \overline{u}^2 = \overline{u^2} - \overline{u}^2. \tag{5.2}$$

Note that the overbar denotes the average over time only.

Here, $\overline{u^2}$ is obtained by averaging the value of u^2 over time, and $\overline{u}^2$ is calculated as a square of an average of u over time. To compute these variables, the values of u and u^2 are stored at every iteration (time step). $\overline{v'^2}$ and $\overline{w'^2}$ are computed in the same way. $\overline{u'v'}$ in equation (5.1) is computed as:

$$\overline{u'v'} = \overline{uv} - \overline{u}\,\overline{v}, \tag{5.3}$$

where the values of uv, u, and v need to be stored at every iteration.

5.2 Wall-Pressure Statistics

In order to analyze the wall-pressure fluctuations, the second, third, and fourth moments of the wall-pressure fluctuations need to be computed.

The wall-pressure mean square is the second moment of the pressure fluctuations and is defined as:

$$\left\langle p'^2 \right\rangle \tag{5.4}$$

where p' is the pressure fluctuations and the brackets $\langle\rangle$ imply the average over the time period and in both the streamwise and spanwise directions. This denotes the intensity of pressure fluctuations. This is computed in the same manner as equation (5.2), except that this value needs to be averaged in the streamwise and spanwise directions as well.

The skewness is the third moment of $p^{'}$ and is normalized by the second moment as:

$$\frac{\left\langle p^{'3} \right\rangle}{\left\langle p^{'2} \right\rangle^{\frac{3}{2}}}. \tag{5.5}$$

If the wall pressure possesses a Gaussian distribution, the skewness should be 0. This means the distribution is symmetric, thus revealing information about the asymmetry of the distribution. To compute $\left\langle p^{'3} \right\rangle$, more information needs to be stored at every iteration. Going through the same analysis as shown in equation (5.2),

$$\overline{p^{'3}} = \overline{p^3} - 3\left(\overline{p^2}\right)\overline{p} + 2\overline{p}^3, \tag{5.6}$$

which requires storage of p^3, p^2, and p at every iteration to complete the average over time.

The flatness, also known as kurtosis, is defined as:

$$\frac{\left\langle p^{'4} \right\rangle}{\left\langle p^{'2} \right\rangle^{2}}, \tag{5.7}$$

which is the fourth moment of $p^{'}$, normalized by the second moment of the perturbations. It is a measure of how important infrequent high-amplitude events are. The distributions with most measurements clustered around the mean will have low flatness. If the distribution is entirely Gaussian, the flatness should be 3. Therefore, values of p^4, p^3, p^2, and p must be stored at every iteration to compute the flatness.

The spatial correlations of the wall-pressure fluctuations are defined in terms of their coherence function:

$$R(\xi,\zeta) = \frac{\langle p'(x,z)p'(x+\xi,z+\zeta)\rangle}{\langle p'^2\rangle} \tag{5.8}$$

where x and z are arbitrary streamwise and spanwise coordinates in the computational domain, and ξ and ζ are the streamwise and spanwise separation distances. The meaningful separation distances are restricted to half of the domain in streamwise and spanwise directions due to the spatial periodicity of the flow.

The time-series data need to be partitioned for optimal sampling of temporal spectra. As suggested in [15], the total time sampling is divided into 12 non-overlapping sections, each with a period $\frac{1}{2}T$ such that $\left(\frac{1}{2}T\right)\frac{u_\tau}{\delta^*} = 2.81$. These 12 sections are then linked to form 11 ensemble units in a way that the first unit includes the first and second sections, the second unit has the second and third sections, and so on. In this way, each ensemble unit has a sequential time history with a period of $T\frac{u_\tau}{\delta^*} = 5.62$ and a minimum frequency resolution $\omega\frac{\delta^*}{u_\tau}$.

The spectra are defined using the Fourier transforms of the windowed wall-pressure fluctuations as:

$$\Phi(\omega,k_x) = C\left\langle\left|\frac{1}{(2\pi)^2}\int_0^T\int_0^{L_x} d(t)\,p'(x,z,t)\,e^{(-i\omega t)}e^{(-ik_x x)}dxdt\right|^2\right\rangle, \tag{5.9}$$

where in this case i denotes a complex number $i = \sqrt{-1}$ (i.e., not a spatial index), T is the time period, d is the windowing function for the time series, and C is the analytic correction factor for

the windowing function as given by Hardin [66]:

$$C = \frac{2\pi}{\int_0^T d^2(t)dt}. \tag{5.10}$$

For the two-dimensional spectrum, the brackets $\langle\rangle$ imply an average over the spanwise direction. According to [67], the data window $d(t)$ in equation (5.11) is computed as:

$$d(t) = \frac{1}{2}\left[1 - cos\left(\frac{t}{T}\right)\right]. \tag{5.11}$$

The data window for the x direction is not needed here, due to the streamwise periodicity of the data.

The one-dimensional temporal spectrum is easily obtained by integrating the two-dimensional spectrum shown in equation (5.9) as:

$$\phi(\omega) = \int_{\infty}^{\infty} \Phi\left(k_x, \omega\right) dk_x. \tag{5.12}$$

It can also be computed by calculating the temporal Fourier transform and taking the streamwise and spanwise average.

These calculations are performed from the simulation and the results are presented in Chapter 6.

CHAPTER 6

NUMERICAL RESULTS

This chapter presents the results using large-eddy simulation and the finite element method formulation that were explained in Chapters 2 and 3, respectively, to solve the turbulent flow on a flat plate. The flow solver incorporates the ability to maintain the turbulent characteristics throughout the simulation, by using the proposed inflow turbulence generation method introduced in Chapter 4. Then the statistics of the wall-pressure fluctuations are calculated as shown in Chapter 5. Results are compared to either empirical results or data from other computations.

6.1 Computational Domain

The domain size, the number of points, and the grid spacings in the streamwise, wall-normal, and spanwise directions are shown in Table 6.1. The mesh statistics of the present work are presented first. For comparison, the same data taken from the work of Lund et al. [46], Singer [15], and Pan et al. [68] are also shown in the table.

The streamwise, wall-normal, and spanwise domain lengths are normalized by δ_{inlet}, the boundary layer thickness at the inlet plane, and are shown first. The number of points in three directions, nx, ny, and nz respectively, are shown next. The last three columns show the grid spacing in each direction, noted as Δx^+, Δy^+_{wall}, and Δz^+. The grid spacings are normalized with

Table 6.1 Mesh statistics of the present work and of the other authors for comparison

Author(s)	$\mathbf{L_x}/\delta_{\mathbf{inlet}}$	$\mathbf{L_y}/\delta_{\mathbf{inlet}}$	$\mathbf{L_z}/\delta_{\mathbf{inlet}}$	**nx**	**ny**	**nz**	Δx^+	Δy^+_{wall}	Δz^+
Present work	10	3	$\frac{\pi}{2}$	102	50	70	65	1.2	15
Lund et al.	29	3	$\frac{\pi}{2}$	290	45	64	64	1.2	15
Singer (low resolution)	5.6	3	1.785	96	64	96	66.7	0.34	21.3
Pan et al.	8	4	2	100	190	50	64	0.4511	32

the viscous scales. These are calculated as:

$$\begin{aligned} \Delta x^+ &= \frac{(u_\tau \Delta x)}{\nu} \\ \Delta y^+_{wall} &= \frac{(u_\tau \Delta y_{wall})}{\nu} \\ \Delta z^+ &= \frac{(u_\tau \Delta z)}{\nu} \end{aligned} \tag{6.1}$$

Note that Δy^+_{wall} is the first grid spacing in the wall-normal direction.

The mesh with 341,481 hexahedral elements has been created in the present work using the statistics shown in Table 6.1 and is displayed in Figure 6.1. The domain is partitioned based on the METIS mesh partitioner [35], and the standard MPI message-passing library [34] for inter-processor communication is used, as mentioned in Chapter 3. The partitioning of the mesh is shown in Figure 6.2. The mesh is first partitioned in the $z = z_{min}$ plane, and then extruded in the z direction. In this way, the nodes in the same x-y coordinates on the "primary" and the "secondary" planes, the $z = z_{max}$ plane and the $z = z_{min}$ plane, respectively, appear on the same processor. This makes the implementation of the periodic boundary conditions explained in Chapter 4 easier.

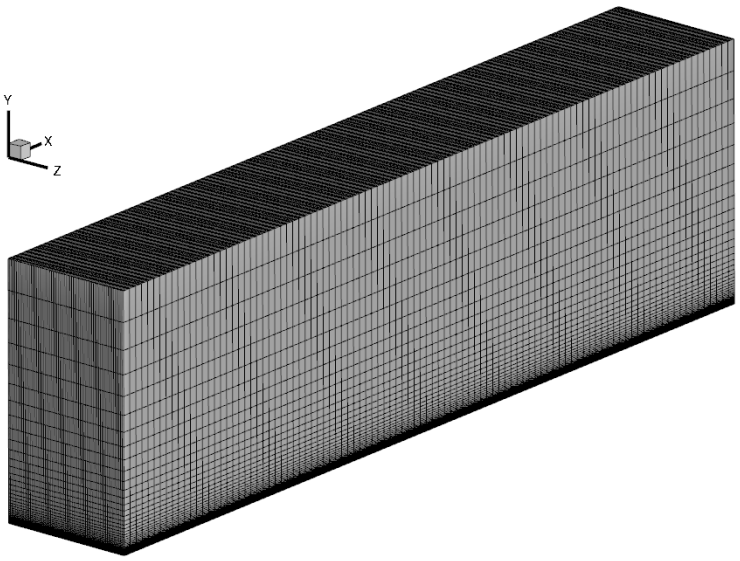

Figure 6.1 Hexahedral mesh

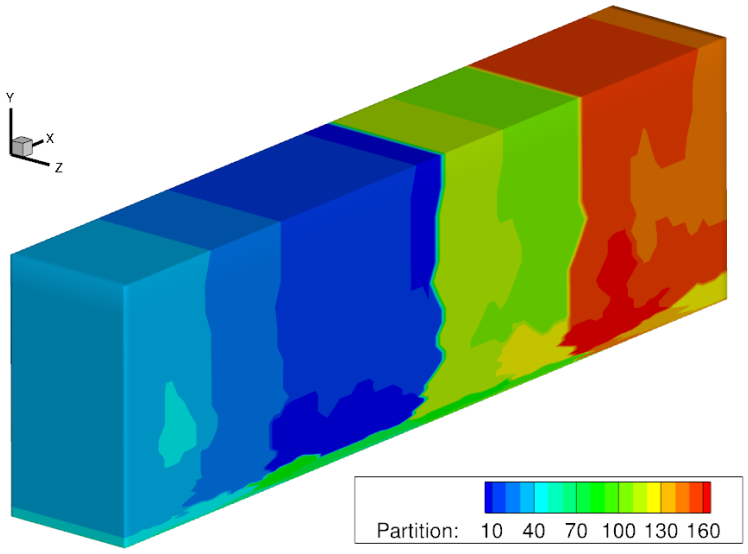

Figure 6.2 Partition of the computational domain with 168 processors

6.2 Results

The flow solver was executed over the computational domain depicted in Section 6.1. In this section, the results from the proposed inflow turbulence generation method are shown first. Then the results for wall-pressure fluctuations statistics and frequency spectra are presented.

6.2.1 Simulation Parameters

The results and calculations were performed for a Mach 0.2 turbulent boundary layer subjected to zero pressure gradients. The parameters of the flow used in this work are shown in Table 6.2.

Table 6.2 Simulation parameters

$\mathbf{M}_\infty$	$\delta_{\mathbf{inlet}}$	$\mathbf{x}_{\mathbf{inlet}}$	$\mathbf{x}_{\mathbf{recycle}}$	$\mathbf{Re}_\theta$	$\mathbf{Re}_{\delta^*}$
0.2	0.1m	0.0 m	0.25742 m	1480	1800

Re_θ here denotes the momentum thickness Reynolds number that is calculated as $Re_\theta = \frac{U_\infty \theta}{\nu_\infty}$. Re_{δ^*} is the Reynolds number based on the inlet displacement thickness (δ^*) and the freestream velocity (U_∞). The simulation has a time step size of $\Delta t = \frac{\delta_{inlet}/U_\infty}{20}$, which is 0.005 (non-dimensional) in this case. A statistically stabilized flow was obtained after 10,000 time steps. Then the results were calculated over the next 20,000 time steps to achieve the turbulence statistics.

6.2.2 Inflow Turbulence Generation Method

The proposed inflow turbulence generation method is validated in this section. The basic idea of generating turbulent inflow data is to estimate the velocity at the inlet of the computational domain, based on the solution at the recycle plane. The velocity field from the recycle plane is extracted, rescaled, and reintroduced at the inlet plane as the boundary condition.

In this work, the mean streamwise velocity field is kept fixed at the inlet, and only the mean velocity fluctuations are extracted from the recycle plane, rescaled, and reintroduced along with the fixed mean velocity profile at the inlet plane. The recycle plane is located at $x_{recycle} \approx 2.5\delta_{inlet}$, which is about 25% of the streamwise length of the domain from the inlet plane. As the recycle plane is located close to the inlet plane, the mirroring method is enforced to prevent the spurious feedback behavior. Figure 6.3 shows the contours of the streamwise velocity field at the initialization and after 15,000 time steps, respectively. Here, x and y are shown in meters, where δ_{inlet} is $0.1m$.

Several slices are taken in the x and y planes, respectively and shown in Figure 6.4. Figure 6.4a shows the velocity contours at the inlet and recycle plane, along with a plane in the middle of the domain ($x \approx 5\delta_{inlet}$). Figure 6.4b shows the contours at (1) near the surface of the flat plate, (2) near the edge of the turbulent boundary, and (3) outside of the turbulent boundary. The streaks are present near the wall in this figure as also presented in the work of Arolla et al. [56].

Figure 6.5 demonstrates the contour plot of $\overline{u'}$ in (x, z)-plane at $y^+ = 2.319$. The same plot is shown in the work of [68]. As expected, the highly elongated regions of high-speed fluid adjacent to the low-speed regions are clearly seen. The coherent structures of these two different

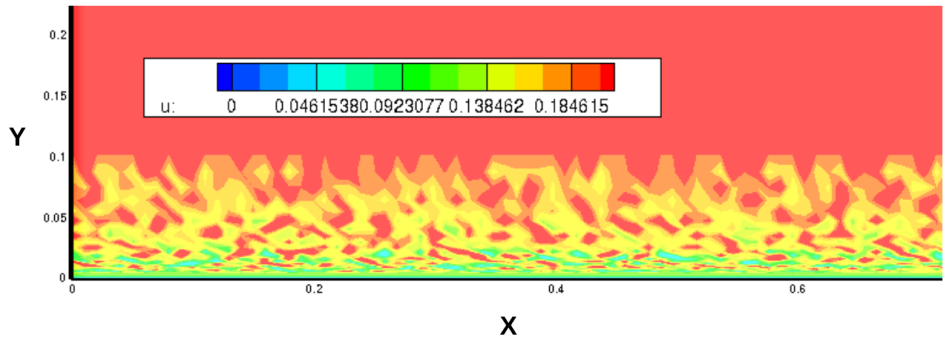

(a) At initialization

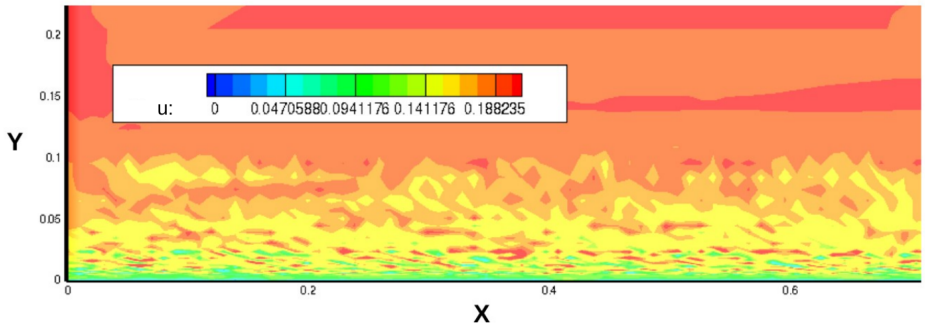

(b) After running simulations

Figure 6.3 Contours of the streamwise velocity u in an x-y plane of the simulation using the modified inflow generation method

speed streaks alternating in the spanwise (z) direction are one of the unique characteristics of the turbulent boundary layer. These streaks decay far from the wall. It is also worth noting that the sponge layer is clearly shown in this figure near the exit of the domain, as the fluctuations should disappear within the sponge region.

These figures indicate that the solutions look correct, qualitatively. The flow stays turbulent throughout the domain, without re-laminarizing. As one of the main challenges of the inflow generation method was to maintain turbulent flow throughout the simulation, these results suggest

that the proposed method appears to be working. However, there isn't anything more dangerous

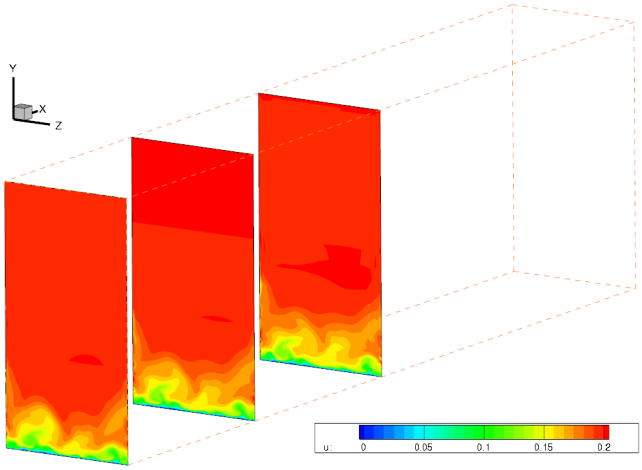

(a) Instantaneous velocity at the inlet plane, at the recycle plane, and in the middle of domain

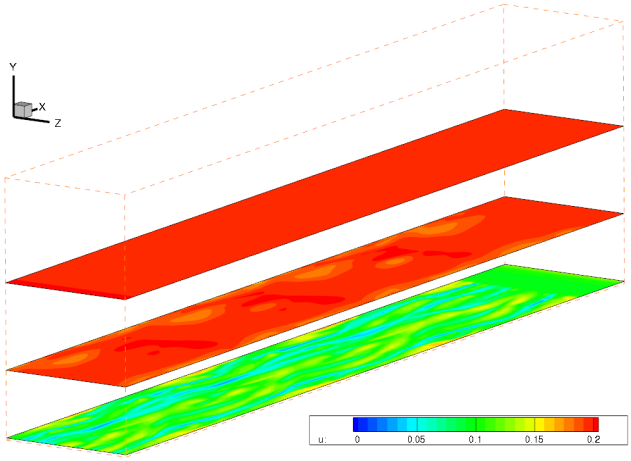

(b) Instantaneous velocity at near the plate, at near the edge of the boundary layer, and outside the boundary layer

Figure 6.4 Contours of instantaneous velocity in the flat plate turbulent boundary layer in different x and y planes in the computational domain (in dashed lines)

than a solution that looks about correct [69]. Therefore, quantification and validation are required before declaring that the proposed method works.

Figure 6.6 shows that all the profiles collapse together to the single curve when using the outer region scaling for the mean streamwise velocity profile and the velocity deficit normalized by the friction velocity, which is an expected result from the turbulent boundary layer theory.

The main challenge of the inflow generation method that was mentioned in Chapter 4 was to keep the friction velocity from continuously decreasing over time. It can be prevented by keeping the mean velocity profile at the inlet and recycling only the fluctuations. The value of u_τ over time at the inlet using this proposed method is shown in Figure 6.7. The target value of friction velocity is $u_\tau \approx 0.046 U_\infty$.

According to Jewkes et al. [58], the friction velocity at the inlet in the original method by Lund et al. [46] goes down to about $u_\tau \approx 0.023 U_\infty$ before it goes back up to the target value.

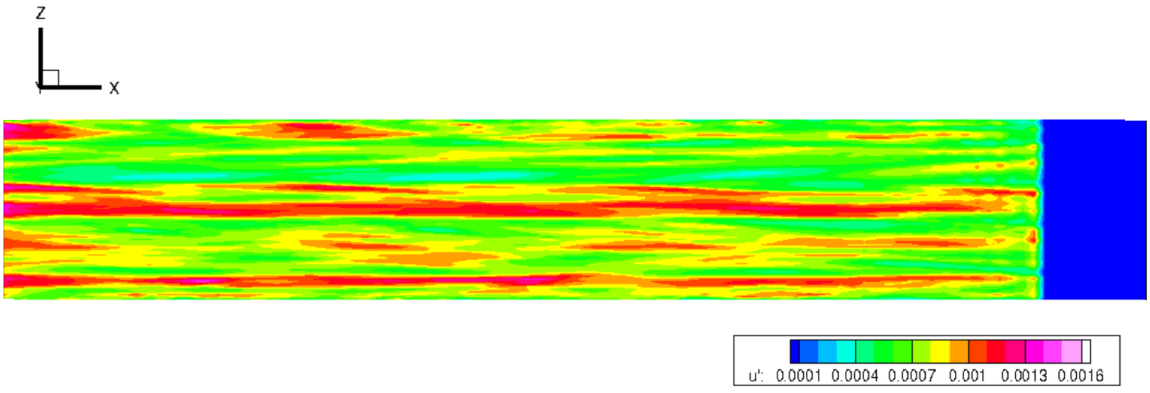

Figure 6.5 The contours of $\overline{u'}$ in (x, z)-plane at $y^+ = 2.319$

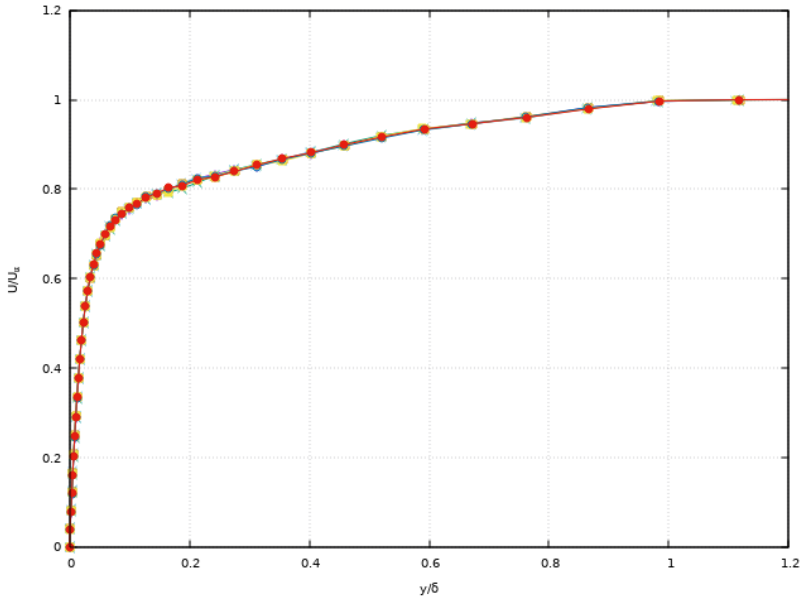

(a) The mean streamwise flow profile (U/U_∞ vs η)

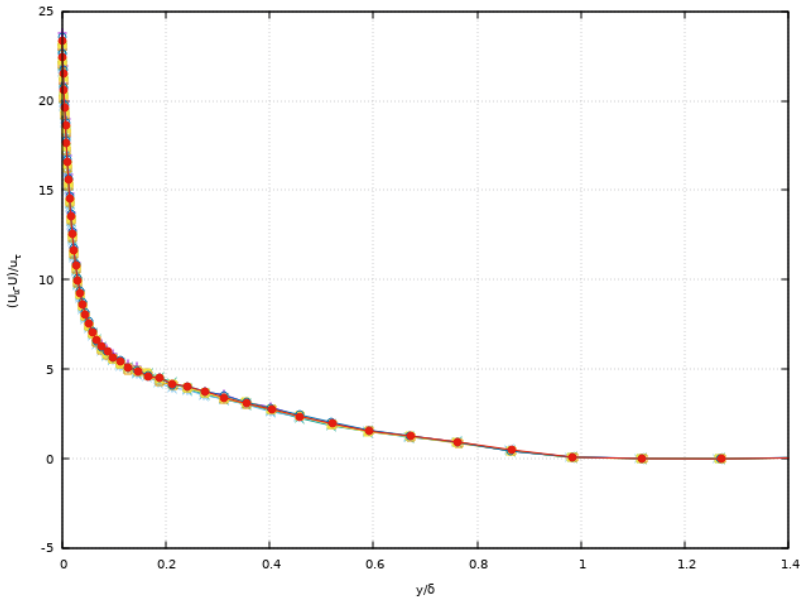

(b) The velocity deficit profile ($(U_\infty - U)/u_\tau$ vs η)

Figure 6.6 The mean streamwise velocity profiles in the outer variable and the velocity deficit normalized by the friction velocity, respectively, at 6 different x-locations (at $x \approx 6.9\delta$, $x \approx 7.2\delta$, $x \approx 7.5\delta$, $x \approx 7.8\delta$, $x \approx 8.1\delta$, and $x \approx 8.4\delta$)

However, as can be seen in Figure 6.7, the friction velocity does not go down as much and stays at around the target value in a stable manner from about 10,000 iterations using the proposed method.

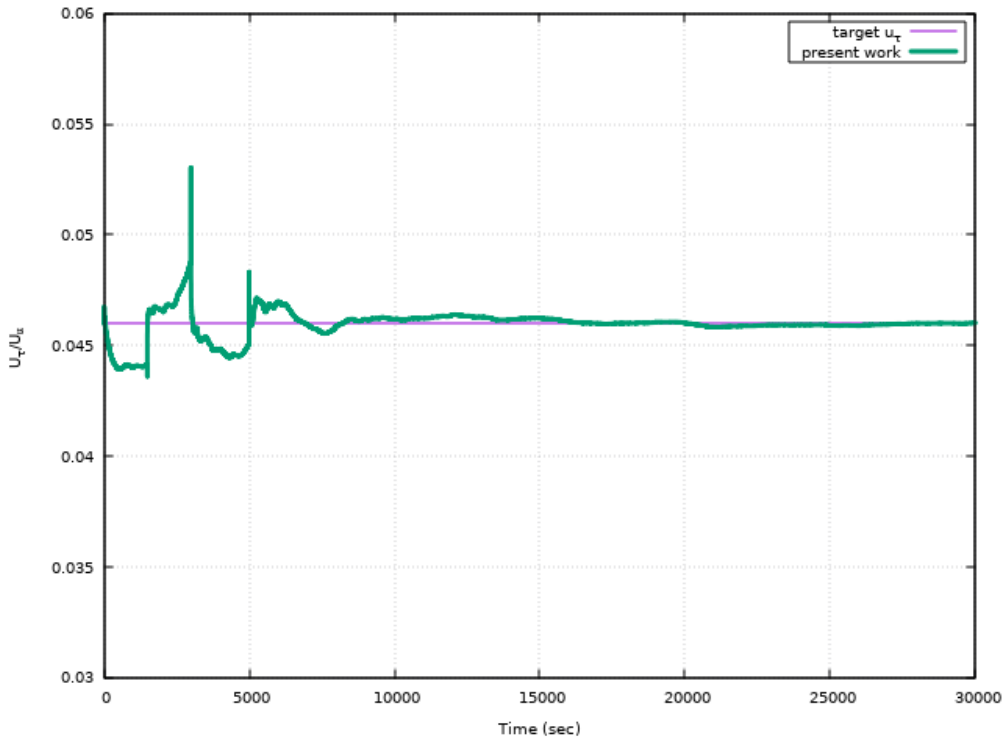

Figure 6.7 The development of the friction velocity u_τ over time at the inlet compared to the target value

The streamwise mean velocity profile that is a result of the proposed inflow turbulence generation method is shown in Figure 6.8 in red. The black line represents $u+ = y+$ for the viscous sublayer which is linear, and the blue line is $u+ = (1/0.4)log(y+) + 5.5$ in the outer layer. The result (in red) agrees well with these functions appropriately, in a way that it clearly shows the viscous sublayer, logarithmic region, and the wake region. The only discrepancy to mention

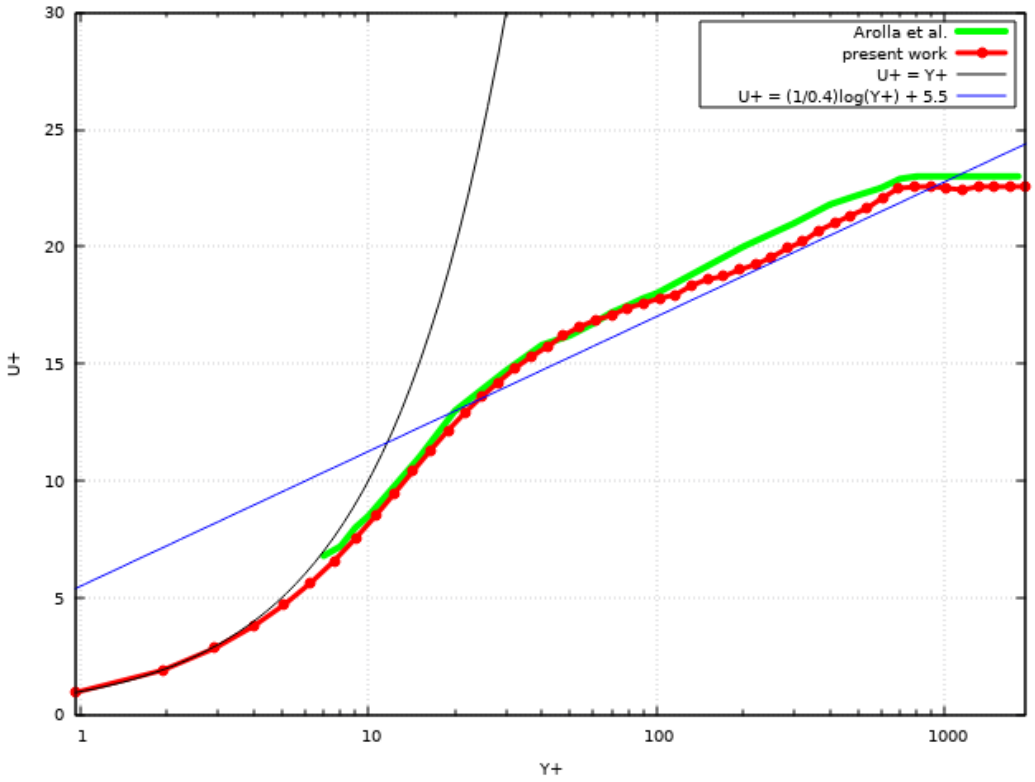

Figure 6.8 The mean streamwise velocity profiles with the theoretical lines compared to the work of Arolla et al. [56]

is that the mean velocity is slightly overpredicted in the logarithmic region. This is also shown in the work of Lund et al., who explained this due to using finite-difference methods on the relatively coarse meshes. The mesh used here is coarser than those employed by Lund et al. [46]; however the reduced dissipation in the finite-element method helps with keeping the profile reasonable. It is anticipated that using high-order spatial integration should improve the agreement.

The u+ vs y+ profile is also compared to that of Arolla et al. [56] which is plotted in green in Figure 6.8. The proposed method agrees well with the analytic functions in black and blue and the agreement is better than that of Arolla et al. [56].

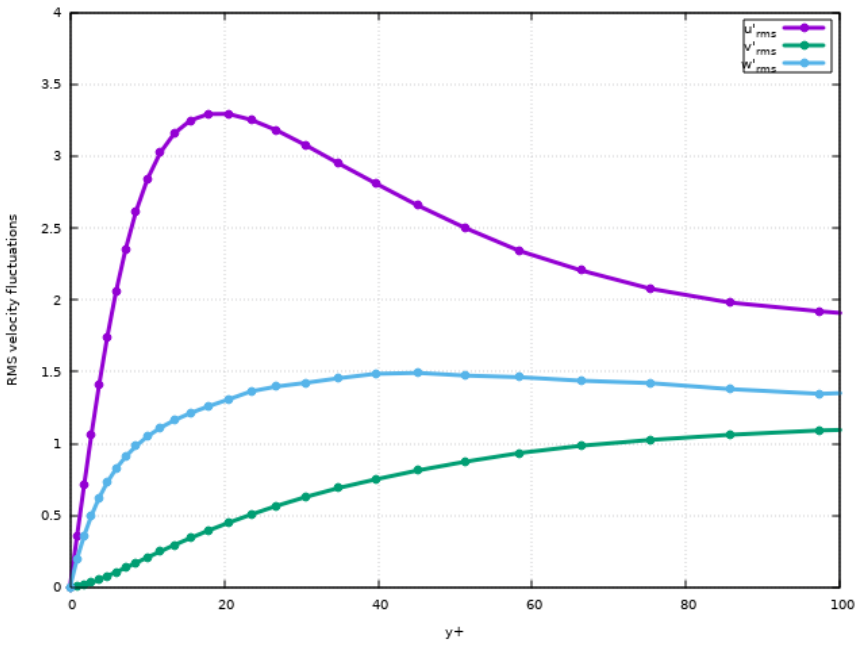

(a) In the inner variables

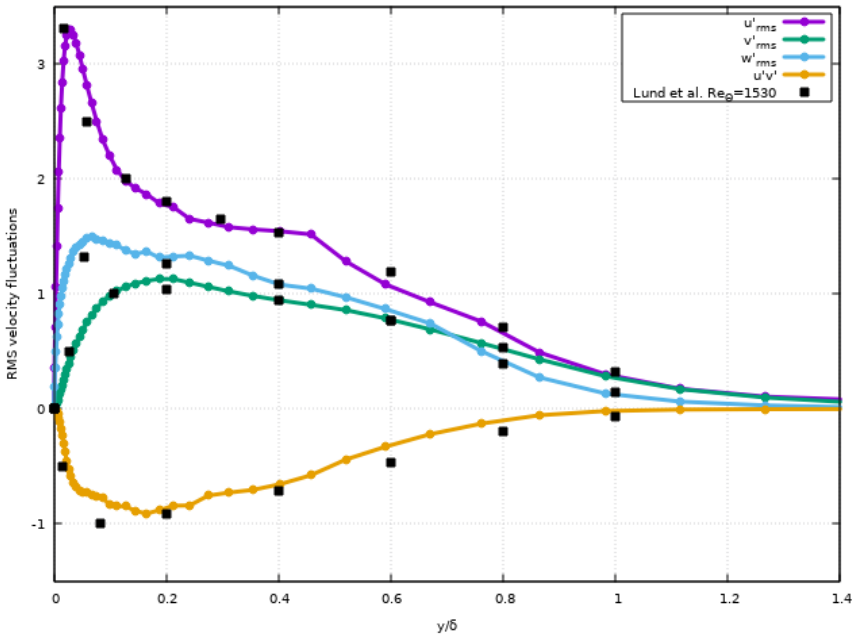

(b) In the outer variables

Figure 6.9 The root mean square velocity fluctuations with sponge layer in the inner and outer variables

The Reynolds stress tensor components, ${u'}_{rms}$, ${v'}_{rms}$, ${w'}_{rms}$, and $u'v'$, are plotted in Figure 6.9 as a function of the inner variables y^+ and the outer variables y/δ, respectively, at the momentum Reynolds number Re_θ=1480. The results extracted from the work of Lund et al. are also shown using the outer variables. Note that the momentum Reynolds number used in the work of Lund et al. is Re_θ=1530.

As expected, the fluctuations peak in the inner layer, and then progressively die out toward the outer boundary layer. Moreover, the streamwise fluctuating component possesses the most turbulence since it is less influenced by the presence of the wall [60]. The wall normal fluctuations are the least turbulent of the normal stresses and the peak is observed further away from the wall. The fact that all three normal components of the Reynolds stress tensor do not go to zero in the free stream right away is due to the intermittency of the turbulent boundary layer. However, the shear stress vanishes, which shows that the flow is more isotropic in the wake region. The RMS velocity fluctuations for all components agree well with the data taken from the work of Lund et al. [46].

In Chapter 4, the sponge layer was introduced. The purpose of the sponge layer was to implement the non-reflecting boundary conditions at the top and outlet planes of the computational domain. Figure 6.10 shows the RMS velocity fluctuations without the sponge layer as a function of the outer variables. It is clear that the reflections from the farfield boundaries are contaminating the solution and the fluctuations are not decaying as expected as one approaches the outer part of the boundary layer. Comparing Figures 6.9 and 6.10, it is obvious that the sponge layer is essential to obtaining the correct turbulent characteristics.

Through these results and observations, it can be concluded that the proposed inflow generation method works well and achieves the purpose of accurately providing the desired turbulent

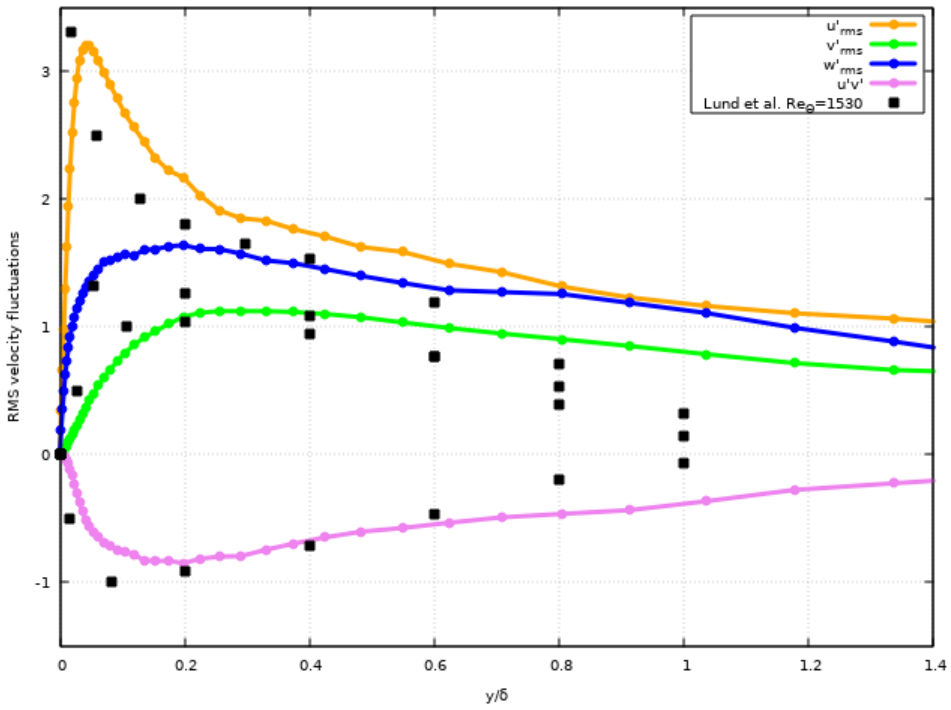

Figure 6.10 The root mean square velocity fluctuations in the outer variable without the sponge layer

characteristics. Therefore, one can extract the wall-pressure statistics from this simulation and compare them to other results.

6.2.3 Wall-Pressure Statistics

6.2.3.1 Time-Averaged Statistics

The time-averaged wall-pressure fluctuations statistics are calculated from the equations introduced in Chapter 5. Table 6.3 is a tabulation of the scalar statistics of the global features of wall-pressure fluctuations from the present work and from the work of others. For the purpose of comparing present results with those of other investigations, the turbulent Reynolds number is

defined as $Re_\tau = u_\tau \delta/\nu$, and is shown in the table. The statistics shown here have been averaged over both time and the streamwise and spanwise directions.

Here, P_{rms} is the square root of the mean square of pressure fluctuations and MS is the mean square of wall-pressure fluctuations. The calculations are explained in Chapter 5. They are normalized here by the time-averaged wall shear τ_ω. The skewness and flatness are also defined in Chapter 5. For comparison, the same data are taken from the work of Singer [15], Pan et al. [68], and Chang et al. [70] and shown in Table 6.3.

Table 6.3 Time-averaged wall pressure statistics including the results of other authors for comparison

Author(s)	**Simulation**	**Re$_\tau$**	**P$_{rms}$**$/\tau_\omega$	**MS**$/\tau_\omega^2$	**Skewness**	**Flatness**
Present work	LES	676	2.661539	7.083792	0.085357	4.883033
Singer	LES (high resolution)	1000	2.74	7.52 ± 0.34	-0.002 ± 0.082	4.74 ± 0.46
Singer	LES (low resolution)	1000	2.60	6.76 ± 0.71	0.036 ± 0.115	4.30 ± 0.51
Pan et al.	LES	800	2.29	5.244	0.185	4.12
Chang et al.	DNS	209	1.71	2.91	0.119	4.99

Note that there are two different results by Singer [15], ensuing from that a result of simulations on two different grid resolutions. Moreover, $\pm$ quantities of his data are the standard deviations in the time sample of spatially averaged quantities.

In order to compare the values of P_{rms}, an equation is taken from the work of Farabee and Casarella [14]. The dependency of P_{rms} on Re_τ is shown in their work and is written as:

$$\frac{P_{rms}^2}{\tau_\omega^2} = \begin{cases} 6.5, & \text{if } Re_\tau \geq 333, \\ 6.5 + 1.86ln(Re_\tau/333), & \text{otherwise.} \end{cases} \tag{6.2}$$

This is plotted in Figure 6.11 in black with the values of P_{rms} from Singer [15], Pan et al. [68], and Chang et al. [70] in blue along with the current work, shown as a red dot. As can be seen from the figure, the value P_{rms} agrees well with the trend line from [14].

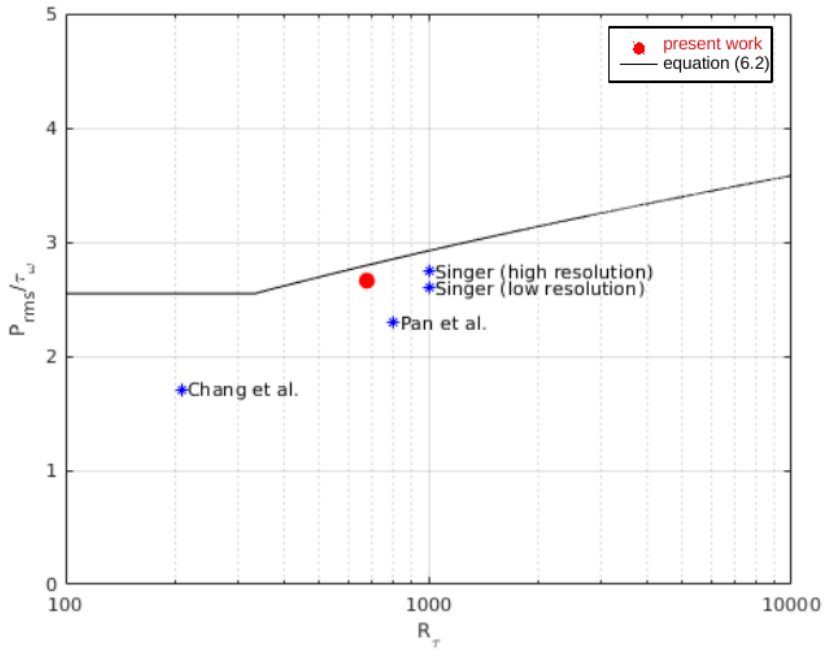

Figure 6.11 Root mean square wall pressure as a function of Reynolds number R_τ, current data in red dot

The skewness indicates the polarity of high amplitude events as mentioned in Chapter 5. Schewe [71] found that the value of skewness using the smallest transducer for measurement was approximately -0.2. He mentioned that when the diameter of the transducer was about 75 wall units, the skewness was almost 0 and remained 0 with larger transducers. Since the resolved structure in the streamwise direction is about 65 wall units, the skewness is expected to approach 0 in this work. Table 6.3 shows that the skewness approaches 0 reasonably, especially when compared to the values from the works of others.

The flatness value obtained from the calculations of this work is about 4.88 as shown in Table 6.3. A Gaussian distribution has a flatness of 3 as mentioned in Chapter 5. This indicates that high-amplitude infrequent events occur more often than with a Gaussian distribution of the wall-pressure distribution. This value is consistent with the values from the work of others. Values given in Table 6.3 show that the distribution of wall-pressure fluctuations in a turbulent boundary layer is clearly not Gaussian.

Figure 6.12 plots the calculations of the streamwise two-point correlation function:

$$\frac{\langle p'(x)p'(x+\xi)\rangle}{\langle p'^2\rangle} \tag{6.3}$$

as functions of the streamwise separation distance in the inner variables ξ^+ and the outer variables ξ/δ^*, respectively.

The calculations from the current work are plotted in red lines, while those from Pan et al. [68] and Singer [15] (high and low resolutions) are shown as symbols. The coherence in the current work goes down and becomes zero before $4\delta^*$, and oscillates around the value of zero.

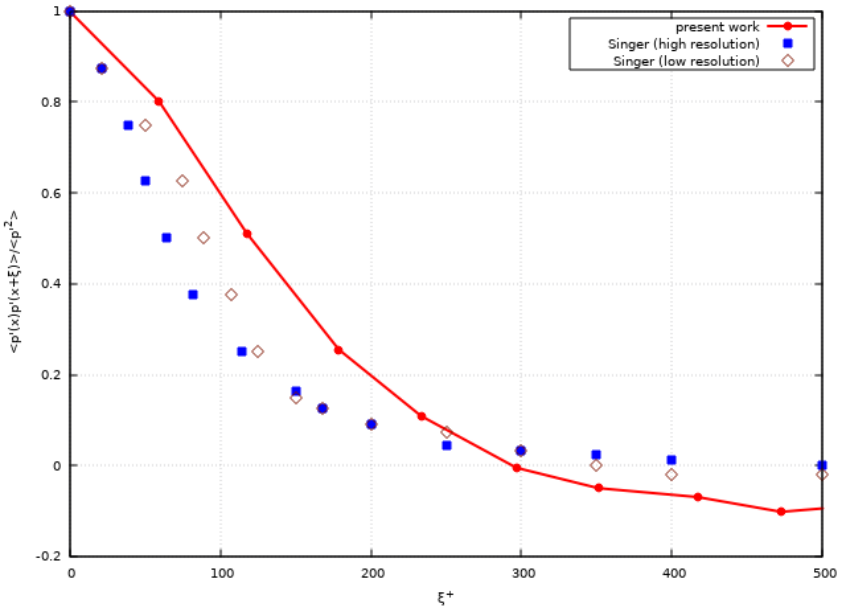

(a) In the inner variables

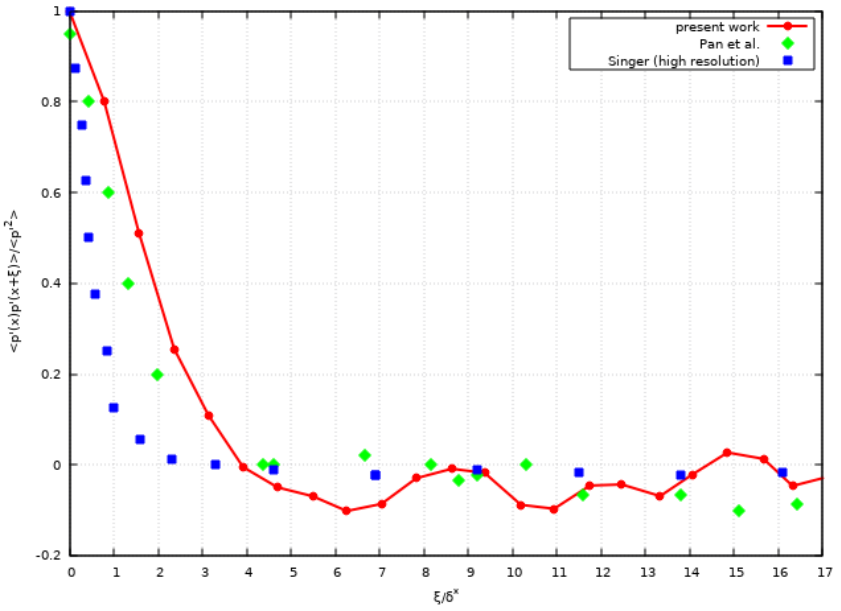

(b) In the outer variables

Figure 6.12 Coherence function of two-point streamwise correlation as functions of two different variables, current data in red line

According to the data reviewed and plotted by Bies [72], the streamwise correlation becomes and remains slightly negative with separation distances greater than approximately $3.5\delta^*$. Singer's data [15] follow this trend the best. In Singer's work [15], it is shown that the details are dependent on the grid resolution. One of the reasons that the current results are not as accurate as that of Singer [15] could be due to the grid resolution. Another reason could be the difference in the turbulent Reynolds number. Re_τ, in the present work, is smaller than the cases of Singer [15] and Pan et al. [68], and from their cases, it can be concluded that as Re_τ gets smaller, the rate at which the correlation drops to zero gets smaller, and it has oscillations with larger amplitudes. Given that the Re_τ in this work is the smallest of all the cases shown here, the trend is consistent with this observation.

Figure 6.13 shows the coherence functions of the two-point spatial correlations for spanwise separations that are calculated as:

$$\frac{\langle p'(z)p'(z+\zeta)\rangle}{\langle p'^2\rangle}, \tag{6.4}$$

as functions of the spanwise separation distance in the inner variables ζ^+ and the outer variables ζ/δ^*, respectively.

The spanwise correlation distance is much larger than the streamwise correlation distance. Within the first few displacement thicknesses, there is a sharp decrease in the coherence function. After that, it becomes and stays at around the value of 0.05 in Singer's case [15]. There are relatively large oscillations in the current work, and the reasons can be, again, the lower mesh resolution or the low turbulent Reynolds number. Nevertheless, the trend is still shown clearly in this figure.

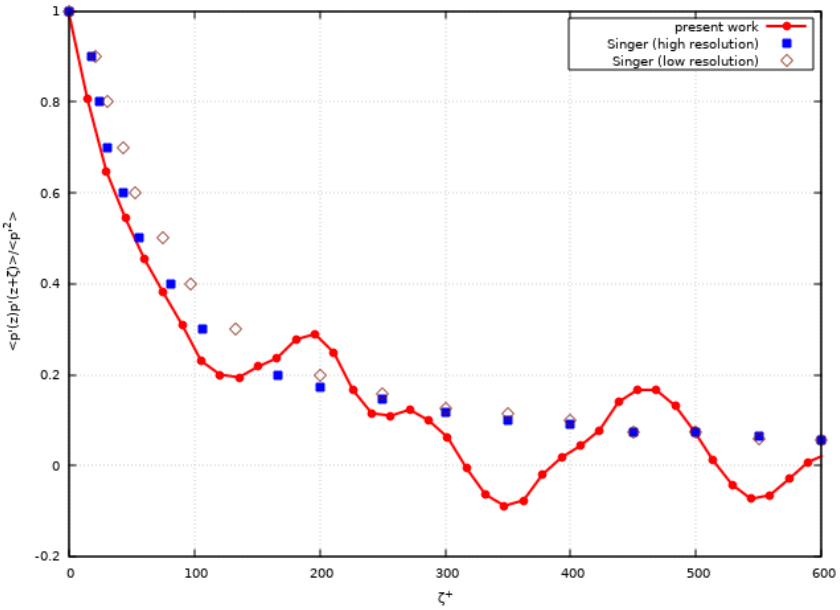

(a) In the inner variables

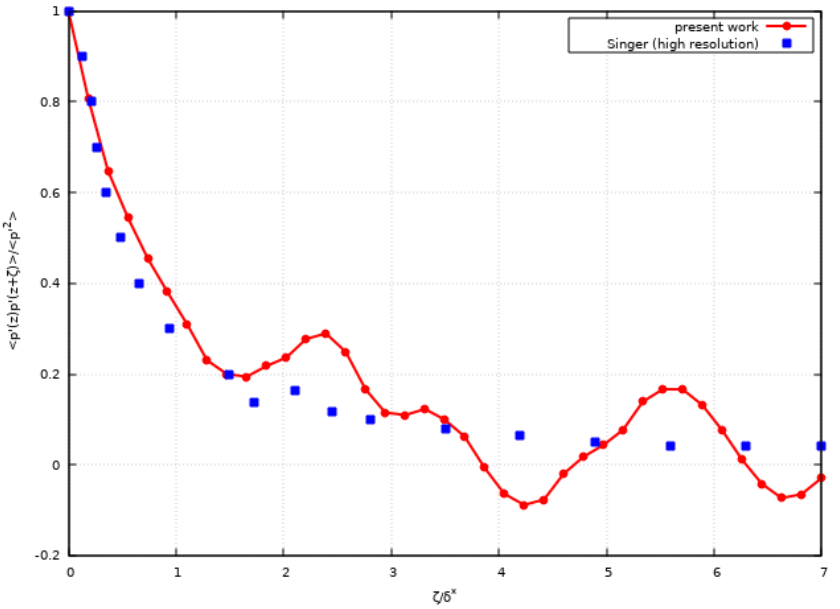

(b) In the outer variables

Figure 6.13 Coherence function of two-point spanwise correlation as functions of two different variables, current data in red line

Overall, the time-averaged wall-pressure statistics of the current work follow the trend as set by other investigations despite the fact that the turbulent Reynolds number is smaller than that of others.

6.2.3.2 1-D Power Spectral Density

The one-dimensional point frequency spectra and the two-dimensional frequency-streamwise-wavenumber spectra are shown to demonstrate that the current solver has a capability to characterize the behavior of the wall-pressure fluctuations. The results are presented in this section.

The one-dimensional power spectral density computed herein is compared with Singer's data [15] and the empirical model by Goody [18] and are shown in Figure 6.14. Goody [18] presented the model of the surface pressure spectrum beneath a two-dimensional, zero-pressure-gradient boundary layer using the experimental wall-pressure spectra measured by seven different research groups. The measurements covered a wide range of Reynolds numbers. He modified the Chase-Howe model [73, 74] for the spectral power density of wall pressure fluctuations $\phi(\omega)$ and proposed the model of the surface pressure spectrum beneath a turbulent boundary layer. The model is shown as:

$$\frac{\phi(\omega) U_\infty}{\tau_\omega^2 \delta} = \frac{C_2 (\omega\delta/U_\infty)^2}{\left[(\omega\delta/U_\infty)^{0.75} + C_1\right]^{3.7} + \left[C_3 R_T^{-0.57} (\omega\delta/U_\infty)\right]^7}, \tag{6.5}$$

where C_1 = 0.5, C_2 = 3.0, and C_3 = 1.1 are empirical constants. R_T is the ratio of the outer to inner boundary layer time scale, and is defined as $R_T = (\delta/U_\infty) / (\nu_\infty/u_\tau^2)$.

Figure 6.14 illustrates the power spectral density as a function of frequency with the current data in red circles; results have been normalized with outer-flow variables.

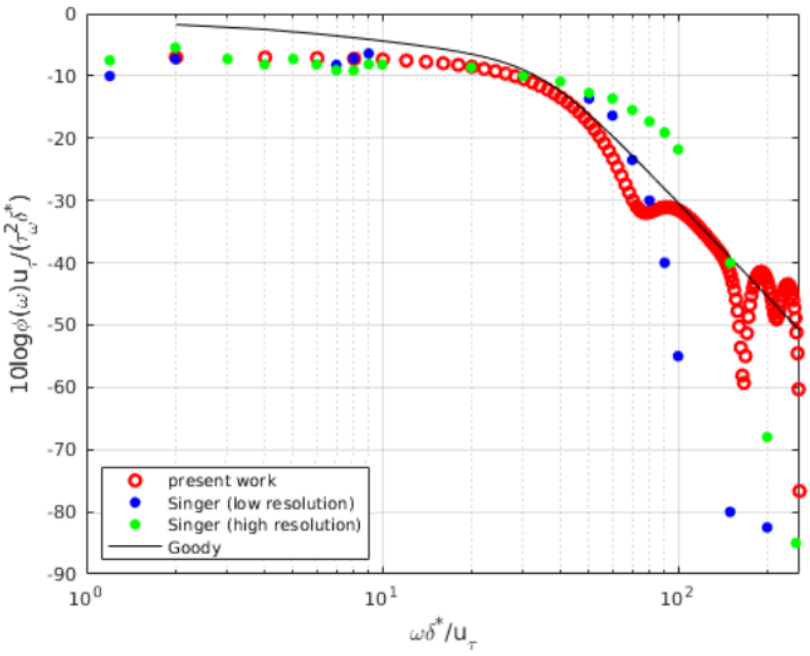

Figure 6.14 The one-dimensional power spectral density as a function of frequency, current data in red circles

Farabee and Casarella [14] measured experimentally the frequency spectra of the wall pressure fluctuations beneath a turbulent boundary layer in a low-noise flow facility. They distinguished three different regimes in the pressure spectral density: low-, high-, and mid-frequency.

Their low-frequency regime [14] where the spectrum scales with ω^2, is where $\omega\delta^*/U_\infty < 0.03$. This corresponds to a very small frequency scale that is below the frequency resolution in the present calculations, so this regime is not captured in the present results.

The high-frequency regime in the work of Farabee and Casarella [14] is observed with rapid decay. Schewe [71] also observed the exponential decay of the spectra at high frequencies. This is clearly observed in the current work as shown in Figure 6.14, despite the fact that certain frequency

ranges appear to be damped significantly compared to others as the frequency gets higher. The reason for this behavior is not yet known.

It can be concluded that the one-dimension power spectral density follows the trend relatively well with the empirical model by Goody [18] and agrees well with the computations of Singer [15].

6.2.3.3 2-D Frequency-Streamwise-Wavenumber Spectral Density

The last result that is presented herein is the two-dimensional spectral density as functions of the frequency and streamwise wavenumber, and are shown in Figure 6.15. f denotes the frequency in Hz and k denotes the streamwise wavenumber in m^{-1}. There are several observations from the contour plot of the spectral density.

First of all, it is observed that the peak of the spectra occurs at the positive wavenumber for different frequencies. This peak is shown as a red line in Figure 6.15b and corresponds to the convection ridge at the specific frequency. Another peak is also found near zero for different frequencies, which is also shown and mentioned in Pan et al. [68].

The convection ridge that is shown at the positive wavenumber (on the right half of the plot) is the high levels region where it starts from the origin and extends to the right half of the plot, as shown in a red line in Figure 6.15b. It is also noted that this convection ridge region is shown only at the low frequencies, and dies out as the frequency increases.

There is another peak, besides the convection ridge, at each frequency near the axis of $k = 0$. This secondary peak is caused by acoustic components and in the acoustic region [68, 75]. At low

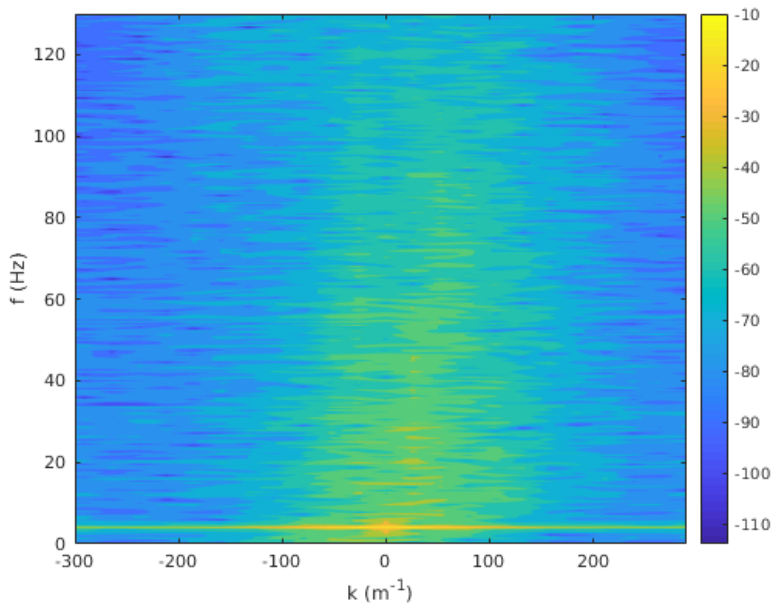

(a) Contours of the spectra

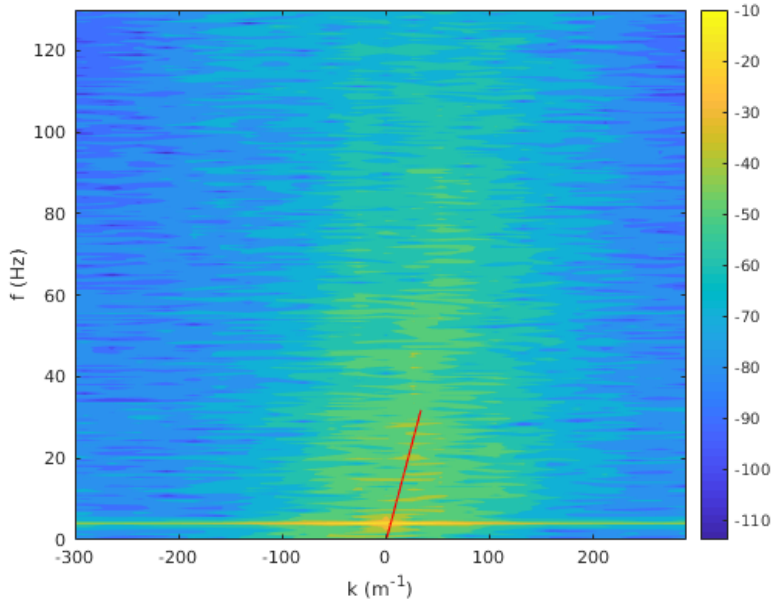

(b) Contours of the spectra with convection ridge shown in red line

Figure 6.15 Contours of the two-dimensional frequency-streamwise-wavenumber spectral density

Mach numbers, the corresponding wavenumber with this secondary peak is $k_0 = \omega/c$ where c is the speed of sound and this value is close to zero.

It is also worth pointing out that there is always a peak when the frequency is about 3$\sim$4 Hz, which corresponds to about 20 rad/sec, regardless of the value of the wavenumber. It is shown as the line parallel to the $k-$axis. Pan et al. [68] presents this in their work and explains this as the peak caused by the motion of the large-scale eddies in the turbulent boundary layer. This shows that the large-eddies at the low frequencies are hardly affected by different wavenumbers.

The two-dimensional frequency-streamwise-wavenumber spectral density shows that the current work possesses the phenomena that are expected in the wall-pressure fluctuations study. Further investigations can be pursued with the current solver to confirm that the wall-pressure fluctuations can be characterized. This will be explained more in Chapter 7.

CHAPTER 7

CONCLUSIONS AND FUTURE WORK

7.1 Conclusions

The turbulent wall-pressure fluctuations have been captured and analyzed in the current work using large-eddy simulation for the large scale motions and a wall-adapting local eddy-viscosity model for the smaller scale motions. The finite element method formulation with the streamwise/upwind Petrov-Galerkin method has been used as the numerical method to solve the governing equations. The proposed inflow generation method with the fixed mean streamwise velocity and the recycled and rescaled velocity fluctuations has been implemented and validated for generating the inflow turbulent velocity profile at the inlet of the computational domain to maintain the turbulent characteristics throughout the simulation. It was necessary to impose non-reflecting boundary conditions at the top and exit of the domain to prevent contamination of the numerical results.

The results on the mean velocity profile and RMS velocity fluctuations presented in this work demonstrate that the turbulent characteristics are captured correctly using a simpler approach than the original recycling and rescaling inflow generation method proposed in [46]. Furthermore, the proposed method prevents the friction velocity from decreasing, as observed by other investigations. Wall-pressure fluctuation characteristics with time-averaged statistics and spectra have

been investigated in the present simulation and agree well with experimental data as well as trends shown from previous efforts.

7.2 Future Work

The work presented in this dissertation uses the finite element method formulation to compute and characterize the wall-pressure fluctuations in the turbulent boundary layer. The next effort to try is to use higher-order finite element method formulations, to perform similar investigations. The finite element method is readily extendable to higher orders, which should produce improved accuracy. Additionally, adaptive mesh refinement (h-, p-, and hp-adaptation) techniques can be explored within the context of the finite element method. In addition, higher-order temporally accurate schemes can also be investigated.

For the inflow generation method used in this work, the same method using different recycle plane locations can be examined to better understand the sensitivity. In the same way, different starting locations of the sponge layer can also be tested to study effects on computed results.

For further investigating the wall-pressure fluctuations, coherence of the cross-spectral density function can be studied as a function of the phase. Moreover, the convection velocity as a function of convection wavenumbers can also be studied.

From the results presented in Section 6.2.3, the same solver that was used in this work needs to be executed on grids with higher mesh resolutions to see if the oscillations shown in the present results are reduced. The same solver using a higher turbulent Reynolds number also needs to be simulated.

REFERENCES

[1] Alaoui, M., *Coherent structures and wall-pressure fluctuations modeling in turbulent boundary layers subjected to pressure gradients*, Ph.D. thesis, Ecole nationale supérieure d'arts et métiers - ENSAM, 2016.

[2] Blake, W. K., *Mechanics of flow-induced sound and vibration*, Vol. II, Academic Press, 1986.

[3] Mixson, J. S. and Wilby, J. F., "Interior Noise," *Aeroacoustics of flight vehicles: theory and practice, volume 2: noise control, NASA reference publication 1258*, Vol. 2, Aug 1991, pp. 271–355.

[4] Kraichnan, R. H., "Pressure fluctuations in turbulent flow over a flat plate," *The Journal of the Acoustical Society of America*, Vol. 28, No. 3, 1956, pp. 378–390.

[5] Spalding, D. B., "A single formula for the law of the wall," *Journal of Applied Mechanics*, Vol. 28, No. 3, 1961, pp. 455–458.

[6] Phillips, O. M., "On the aerodynamic surface sound from a plane turbulent boundary layer," *Proceedings of the Royal Society of London A: Mathematical, Physical and Engineering Sciences*, Vol. 234, No. 1198, 1956, pp. 327–335.

[7] Willmarth, W. W. and Wooldridge, C. E., "Measurements of the fluctuating pressure at the wall beneath a thick turbulent boundary layer," *Journal of Fluid Mechanics*, Vol. 14, No. 2, 1962, pp. 187–210.

[8] Corcos, G. M., "Resolution of pressure in turbulence," *The Journal of the Acoustical Society of America*, Vol. 35, No. 2, 1963, pp. 192–199.

[9] Corcos, G. M., "The structure of the turbulent pressure field in boundary-layer flows," *Journal of Fluid Mechanics*, Vol. 18, No. 3, 1964, pp. 353–378.

[10] Blake, W. K., "Turbulent boundary-layer wall-pressure fluctuations on smooth and rough walls," *Journal of Fluid Mechanics*, Vol. 44, No. 4, 1970, pp. 637–660.

[11] Willmarth, W. W., "Pressure fluctuations beneath turbulent boundary layers," *Annual Review of Fluid Mechanics*, Vol. 7, No. 1, 1975, pp. 13–36.

[12] Kim, J., "On the structure of pressure fluctuations in simulated turbulent channel flow," *Journal of Fluid Mechanics*, Vol. 205, 1989, pp. 421–451.

[13] Choi, H. and Moin, P., "On the space-time characteristics of wall-pressure fluctuations," *Physics of Fluids A: Fluid Dynamics*, Vol. 2, No. 8, 1990, pp. 1450–1460.

[14] Farabee, T. M. and Casarella, M., "Spectral features of wall pressure fluctuations beneath turbulent boundary layers," *Physics of Fluids A: Fluid Dynamics*, Vol. 3, No. 10, 1991, pp. 2410–2420.

[15] Singer, B. A., "Large-eddy simulation of turbulent wall-pressure fluctuations," *NASA Contract Report, 198276*, 1996.

[16] Chang III, P., Piomelli, U., and Blake, W., "Relationship between wall pressure and velocity-field sources," *Physics of Fluids*, Vol. 11, No. 11, 1999, pp. 3434–3448.

[17] Wang, M., "Dynamic wall modeling for LES of complex turbulent flows," *Annual Research Briefs, CTR, Standford University*, 2000, pp. 241–250.

[18] Goody, M., "Empirical spectral model of surface pressure fluctuations," *AIAA Journal*, Vol. 42, No. 9, 2004, pp. 1788–1794.

[19] Lee, Y., Blake, W., and Farabee, T., "Prediction of wall pressure spectrum using a RANS calculation," *43rd AIAA Aerospcae Sciences Meeting and Exhibit*, January 2005.

[20] Mahmoudnejad, N. and Hoffmann, K., "Numerical computation of wall pressure fluctuations due to a turbulent boundary layer," *49th AIAA Aerospace Sciences Meeting including the New Horizons Forum and Aerospace Exposition*, January 2011.

[21] Marshak, A. and Davis, A., *3D radiative transfer in cloudy atmospheres*, Springer-Verlag Berlin Heidelberg, 2005.

[22] Davidson, P. A., *Turbulence: an introduction for scientists and engineers*, Oxford University Press, 2004.

[23] Briley, W. R., Private Correspondence, 2013.

[24] Wilcox, D. C., *Turbulence modeling for CFD*, DCW Industries, 2nd edition, 1998.

[25] Nicoud, F. and Ducros, F., "Subgrid-scale stress modelling based on the square of the velocity gradient tensor," *Flow, Turbulence and Combustion*, Vol. 62, No. 3, September 1999, pp. 183–200.

[26] Wang, L., Anderson, K., Kapadia, S., and Taylor, L., "Multiscale large eddy simulation of turbulence using high order finite element methods," *AIAA AVIATION 2014 -7th AIAA Theoretical Fluid Mechanics Conference*, June 2014.

[27] Vreman, B., Geurts, B., and Kuerten, H., "A priori tests of large eddy simulation of the compressible plane mixing layer," *Journal of Engineering Mathematics*, Vol. 29, No. 4, Jul 1995, pp. 299–327.

[28] White, F. M., *Viscous fluid flow*, McGraw-Hill, 2006.

[29] Ma, J., Wang, F., and Tang, X., "Comparison of several subgrid-scale models for large-eddy simulation of turbulent flows in water turbine," *Fluid Machinery and Fluid Mechanics*, Springer Berlin Heidelberg, Berlin, Heidelberg, 2009, pp. 328–334.

[30] Erwin, J. T., *Stabilized finite elements for compressible turbulent Navier-Stokes*, Ph.D. thesis, University of Tennessee at Chattanooga, 2013.

[31] Wang, L. and Mavriplis, D. J., "Implicit solution of the unsteady Euler equations for high-order accurate discontinuous Galerkin discretizations," *Journal of Computational Physics*, Vol. 225, No. 2, 2007, pp. 1994 – 2015.

[32] Saad, Y. and Schultz, M. H., "GMRES: A generalized minimal residual algorithm for solving nonsymmetric linear systems," *SIAM Journal on Scientific and Statistical Computing*, Vol. 7, No. 3, 1986, pp. 856–869.

[33] Saad, Y., *Iterative methods for sparse linear systems*, Society for Industrial and Applied Mathematics, 2nd ed., 2003.

[34] Gropp, W., Lusk, E., and Skjellum, A., *Using MPI: portable parallel programming with the message passing interface*, MIT Press, Cambridge, MA, 1994.

[35] Karypis, G., "METIS, University of Minnesota, Department of Computer Science," http://www-users.cs.umn.edu/karypis/metis.

[36] Rai, M. M. and Moin, P., "Direct numerical simulation of transition and turbulence in a spatially evolving boundary layer," *Journal of Computational Physics*, Vol. 109, No. 2, 1993, pp. 169–192.

[37] Xiao, F., Dianat, M., and McGuirk, J. J., "An LES turbulent inflow generator using a recycling and rescaling method," *Flow, Turbulence and Combustion*, Vol. 98, No. 3, Apr 2017, pp. 663–695.

[38] Tabor, G. R. and Baba-Ahmadi, M. H., "Inlet conditions for large eddy simulation: A review," *Computers & Fluids*, Vol. 39, No. 4, 2010, pp. 553 – 567.

[39] Bazdidi-Tehrani, F., Kiamansouri, M., and Jadidi, M., "Inflow turbulence generation techniques for large eddy simulation of flow and dispersion around a model building in a turbulent atmospheric boundary layer," *Journal of Building Performance Simulation*, Vol. 9, No. 6, 2016, pp. 680–698.

[40] Wu, X., "Inflow turbulence generation nethods," *Annual Review of Fluid Mechanics*, Vol. 49, No. 1, 2017, pp. 23–49.

[41] Aider, J. L., Danet, A., and Lesieur, M., "Large-eddy simulation applied to study the influence of upstream conditions on the time-dependant and averaged characteristics of a backward-facing step flow," *Journal of Turbulence*, Vol. 8, 2007, pp. 1–30.

[42] Wang, D., Yu, X., Zhou, Y., and Tse, T. K. T., "A combination method to generate fluctuating boundary conditions for large eddy simulation," *Wind and Structures*, Vol. 20, No. 4, 2015, pp. 579–607.

[43] Kim, Y., Castro, I. P., and Xie, Z. T., "Divergence-free turbulence inflow conditions for large-eddy simulations with incompressible flow solvers," *Computers & Fluids*, Vol. 84, 2013, pp. 56 – 68.

[44] Perret, L., Delville, J., Manceau, R., and Bonnet, J., "Turbulent inflow conditions for large-eddy simulation based on low-order empirical model," *Physics of Fluids*, Vol. 20, No. 7, 2008, pp. 1–17.

[45] Penttinen, O. and Nilsson, H., "A fully synthetic turbulent boundary condition with a homogeneous vortex distribution," *Computer Physics Communications*, Vol. 190, 2015, pp. 23 – 32.

[46] Lund, T. S., Wu, X., and Squires, K. D., "Generation of turbulent inflow data for spatially-developing boundary layer simulations," *Journal of Computational Physics*, Vol. 140, No. 2, 1998, pp. 233 – 258.

[47] Spalart, P. R. and Leonard, A., "Direct numerical simulation of equilibrium turbulent boundary layers," *Turbulent Shear Flows 5*, Springer Berlin Heidelberg, Berlin, Heidelberg, 1987, pp. 234–252.

[48] Karman, T. V., "Mechanical similitude and turbulence," *National Advisory Committee on Aeronautics*, 1931.

[49] Mikhailov, V. V., "Universal velocity defect law for the turbulent boundary layer," *Fluid Dynamics*, Vol. 40, No. 2, 2005, pp. 245 – 255.

[50] Garnier, E., Adams, N., and Sagaut, P., *Large Eddy Simulation for Compressible Flows*, Springer, 2009.

[51] Klein, M., Sadiki, A., and Janicka, J., "A digital filter based generation of inflow data for spatially developing direct numerical or large eddy simulations," *Journal of Computational Physics*, Vol. 186, No. 2, 2003, pp. 652 – 665.

[52] Keating, A., Piomelli, U., Balaras, E., and Kaltenbach, H., "A priori and a posteriori tests of inflow conditions for large-eddy simulation," *Physics of Fluids*, Vol. 16, No. 12, 2004, pp. 4696–4712.

[53] Ferrante, A. and Elghobashi, S., "A robust method for generating inflow conditions for direct simulations of spatially-developing turbulent boundary layers," *Journal of Computational Physics*, Vol. 198, No. 1, 2004, pp. 372 – 387.

[54] Liu, K. and Pletcher, R. H., "Inflow conditions for the large eddy simulation of turbulent boundary layers: a dynamic recycling procedure," *Journal of Computational Physics*, Vol. 219, No. 1, 2006, pp. 1 – 6.

[55] Simens, M. P., Jimenez, J., Hoyas, S., and Mizuno, Y., "A high-resolution code for turbulent boundary layers," *Journal of Computational Physics*, Vol. 228, No. 11, 2009, pp. 4218 – 4231.

[56] Arolla, S. K. and Durbin, P. A., "Generating inflow turbulence for eddy simulation of turbomachinery flows," *52nd Aerospace Sciences Meeting, AIAA SciTech Forum*, January 2014.

[57] Spalart, P. R., Strelets, S., and Travin, A., "Direct numerical simulation of large-eddy-break-up devices in a boundary layer," *International Journal of Heat and Fluid Flow"*, Vol. 27, No. 5, 2006, pp. 902 – 910.

[58] Jewkes, J. W., Chung, Y. M., and Carpenter, P. W., "Modification to a turbulent inflow generation method for boundary layer flows," *AIAA Journal*, Vol. 49, January 2011, pp. 247–250.

[59] Liu, K. and Pletcher, R. H., "A procedure to establish inflow conditions for LES of spatially developing turbulent boundary layers," *ASME 2004 Heat Transfer/Fluids Engineering Summer Conference*, Vol. 2, No. Part A and B, Jul 2004, pp. 1091–1099.

[60] Bohr, E., Bailon-Cuba, J., Jansen, K., and Castillo, L., "Inflow generation technique for large eddy simulation using equilibrium similarity analysis," *4th AIAA Theoretical Fluid Mechanics Meeting*, June 2005.

[61] Araya, G., Castillo, L., Meneveau, C., and Jansen, K., "A dynamic multi-scale approach for turbulent inflow boundary conditions in spatially developing flows," *Journal of Fluid Mechanics*, Vol. 670, 2011, pp. 581–605.

[62] Spille-Kohoff, A. and Kaltenbach, H., "Generation of Turbulent Inflow Data with a Prescribed Shear-Stress Profile," *DNS/LES Progress and Challenges*, 08 2001.

[63] Nikitin, N., "Spatial periodicity of spatially evolving turbulent flow caused by inflow boundary condition," *Physics of Fluids*, Vol. 19, No. 9, 2007, pp. 091703.

[64] Fujima, S., Fukasawa, Y., and Tabata, M., "Finite element formulation of periodic conditions and numerical observation of three-dimensional behavior in a flow," 1993, pp. 113–119.

[65] El-Askary, W., "Large eddy simulation of turbulent-supersonic boundary layer subjected to multiple distortions," *CMES. Computer Modeling in Engineering & Sciences*, Vol. 74, 2011.

[66] Hardin, J., "Introduction to time series analysis," *NASA Ref. Pub. 1145*, 1990.

[67] Press, W. H., Teukolsky, S. A., Vetterling, W. T., and Flannery, B. P., *Numerical recipes in C (2Nd Ed.): The art of scientific computing*, Cambridge University Press, New York, NY, USA, 1992.

[68] Pan, Y. and Zhang, H., "Investigation of wall pressure flucatutions in a turbulent boundary layer by Large Eddy Simulation," *Journal of Shanghai Jiaotong University*, Vol. 12, No. 6, 2007, pp. 817–823.

[69] Swafford, T. W., Private Correspondence, 2013.

[70] Chang III, P., Abraham, B. M., and Piomelli, U., "Wavenumber-frequency characteristics of wall pressure fluctuations computed using turbulence simulations," *ASME, Active Control of Vibration and Noise*, Vol. 11, No. 11, 1994, pp. 229–244.

[71] Schewe, G., "On the structure and resolution of wall-pressure fluctuations associated with turbulent boundary-layer flow," *Journal of Fluid Mechanics*, Vol. 134, 1983, pp. 311–328.

[72] Bies, D. A., "A review of flight and wind tunnel measurements of boundary layer pressure fluctuations and induced structural response," *NASA CR-626*, 1996.

[73] Chase, D., "Modeling the wavevector-frequency spectrum of turbulent boundary layer wall pressure," *Journal of Sound and Vibration*, Vol. 70, No. 1, 1980, pp. 29–67.

[74] Howe, M. S., *Acoustics of Fluid-Structure Interactions*, Cambridge Monographs on Mechanics, Cambridge University Press, 1998.

[75] Howe, M. S., "Surface pressures and sound produced by turbulent flow over smooth and rough walls," *The Journal of the Acoustical Society of America*, Vol. 90, No. 2, 1991, pp. 1041–1047.

VITA

Jhiin Joo was born in Daegu, South Korea. She earned her Bachelor's degree in Electrical Engineering and Computer Science from the Kyungpook National University, and her Master's degree in Electrical Engineering from the University of Southern California. She received a Ph.D. in Computational Engineering from the University of Tennessee at Chattanooga in August 2019.